

## MAGII-CAT IV. KINEMATICS OF THE CIRCUMGALACTIC MEDIUM AND EVIDENCE FOR QUIESCENT EVOLUTION AROUND RED GALAXIES

NIKOLE M. NIELSEN<sup>1,2</sup>, CHRISTOPHER W. CHURCHILL<sup>2</sup>, GLENN G. KACPRZAK<sup>1</sup>, MICHAEL T. MURPHY<sup>1</sup>, AND JESSICA L. EVANS<sup>2</sup>

<sup>1</sup> Centre for Astrophysics and Supercomputing, Swinburne University of Technology, Hawthorn, Victoria 3122, Australia; nikolenielsen@swin.edu.au

<sup>2</sup> Department of Astronomy, New Mexico State University, Las Cruces, NM 88003, USA

Accepted by ApJ, January 8, 2016

### ABSTRACT

The equivalent widths of Mg II absorption in the circumgalactic medium (CGM) trace the global star formation rate up to  $z < 6$ , are larger for star-forming galaxies than passively-evolving galaxies, and decrease with increasing distance from the galaxy. We delve further into the physics involved by investigating gas kinematics and cloud column density distributions as a function of galaxy color, redshift, and projected distance from the galaxy (normalized by galaxy virial radius,  $D/R_{\text{vir}}$ ). For 39 isolated galaxies at  $0.3 < z_{\text{gal}} < 1.0$ , we have detected Mg II absorption in high-resolution ( $\Delta v \simeq 6.6 \text{ km s}^{-1}$ ) spectra of background quasars within a projected distance of  $7 < D < 190 \text{ kpc}$ . We characterize the absorption velocity spread using pixel-velocity two-point correlation functions. Velocity dispersions and cloud column densities for blue galaxies do not differ with redshift nor with  $D/R_{\text{vir}}$ . This suggests that outflows continually replenish the CGM of blue galaxies with high velocity dispersion, large column density gas out to large distances. Conversely, absorption hosted by red galaxies evolves with redshift where the velocity dispersions (column densities) are smaller (larger) at  $z_{\text{gal}} < 0.656$ . After taking into account larger possible velocities in more massive galaxies, we find that there is no difference in the velocity dispersions or column densities for absorption hosted by red galaxies with  $D/R_{\text{vir}}$ . Thus, a lack of outflows in red galaxies causes the CGM to become more quiescent over time, with lower velocity dispersions and larger column densities towards lower  $z_{\text{gal}}$ . The quenching of star formation appears to affect the CGM out to  $D/R_{\text{vir}} = 0.75$ .

*Keywords:* galaxies: halos — quasars: absorption lines

### 1. INTRODUCTION

Through extensive observations and detailed simulations, it has become clear that the baryon cycle plays a key role in governing the evolution of galaxies (e.g., [Oppenheimer & Davé 2008](#); [Lilly et al. 2013](#)). In this scenario, galaxies grow by accreting pristine gas from the intergalactic medium (IGM), which is the fuel for star formation. Intense star formation and/or supernovae then drive outflowing galactic-scale winds, entraining portions of the interstellar medium (ISM) and coplanar gas along the way. Serving as the interface between the IGM and the ISM, the circumgalactic medium (CGM) contains the gas that has yet to accrete onto the galaxy itself and stores outflowing material until it re-accretes onto the galaxy. The CGM is also massive, with estimates of  $M_{\text{CGM}} > 10^9 M_{\odot}$  for  $\sim L_*$  galaxies ([Thom et al. 2011](#); [Tumlinson et al. 2011](#); [Werk et al. 2013](#)), a gas mass comparable to the gas in galaxies themselves (i.e., the ISM).

The CGM has been studied extensively by using quasar absorption lines in which a background quasar sightline pierces the CGM within a few hundred kiloparsecs projected on the sky. Much of this work has been focused on Mg II  $\lambda\lambda 2796, 2803$  absorption (e.g., [Bergeron & Boissé 1991](#); [Steidel et al. 1994](#); [Guillemin & Bergeron 1997](#); [Steidel et al. 1997](#); [Barton & Cooke 2009](#); [Chen et al. 2010](#); [Kacprzak et al. 2011](#); [Lan et al. 2014](#)), which is observable from the ground at optical wavelengths over a large redshift range ( $0.1 < z < 2.5$ ). Mg II has been found to trace two critical components of the baryon cycle: accretion (e.g., [Steidel et al. 2002](#); [Kacprzak et al. 2010](#); [Ribaud et al. 2011](#); [Kacprzak et al. 2012b](#); [Martin et al. 2012](#); [Rubin et al. 2012](#); [Bouché et al. 2013](#); [Crighton et al. 2013](#)) and galactic-scale outflowing winds. (e.g., [Weiner et al. 2009](#); [Rubin et al. 2010](#),

[2014](#); [Bouché et al. 2012](#); [Martin et al. 2012](#); [Bordoloi et al. 2014a,b](#); [Kacprzak et al. 2014](#)).

Determining which aspect of the baryon cycle Mg II absorbers trace has thus far required examining the velocities of the gas with respect to the galaxy systemic velocity. For example, the signatures of accreting and/or rotating gas include absorption that is located to one side (i.e., entirely bluewards or redwards) of the galaxy systemic velocity ([Steidel et al. 2002](#); [Kacprzak et al. 2010](#); [Stewart et al. 2011](#); [Bouché et al. 2013](#)) or observing redshifted absorption with respect to the galaxy systemic velocity in a “down-the-barrel” approach ([Martin et al. 2012](#); [Rubin et al. 2012](#)). Outflows are commonly observed as blueshifted absorption (with respect to the galaxy systemic velocity) for the same down-the-barrel approach (e.g. [Weiner et al. 2009](#); [Rubin et al. 2010, 2014](#); [Martin et al. 2012](#); [Bordoloi et al. 2014b](#)). Recently, [Fox et al. \(2015\)](#) found a quasar whose sightline passes through the “Fermi bubbles” located near the center of the Milky Way Galaxy. In low ionization absorption, they found velocity structure in the form of smaller column density, higher velocity components that were consistent with the front and back sides of the Fermi bubbles. This result provides hints that the velocity structure of the absorbers themselves, rather than just the velocity with respect to the galaxy, is dependent on baryon cycle processes.

Other works have alluded to the kinematic properties of the absorption itself in the presence of outflows by examining only the Mg II equivalent width,  $W_r(2796)$ . This method finds that  $W_r(2796)$  is dependent on galaxy color (star formation rate), azimuthal angle, and/or inclination, where larger values tend to be associated with blue galaxies and sightlines probing galaxies near their minor axes ([Bordoloi et al. 2011](#),

2014a; Kacprzak et al. 2011, 2012a; Bouché et al. 2012), both of which are known to host bipolar outflows. Given that  $W_r(2796)$  correlates with the number of clouds or Voigt profile components (Petitjean & Bergeron 1990; Churchill et al. 2003; Evans 2011), this indicates that either the column densities, velocity spreads, or both are larger in the presence of outflows. The kinematics and column densities may also differ when associated with accretion, though accreting gas is harder to detect due to its small covering fraction ( $\sim 6\%$ ; Martin et al. 2012), and the fact that outflowing gas dominates the absorption signal.

Using  $\sim 8500$  strong Mg II absorbers ( $0.7 < W_r(2796) < 6.0 \text{ \AA}$ ) at  $0.4 < z < 1.3$ , Ménard et al. (2011) found a  $15\sigma$  correlation between  $W_r(2796)$  and the [O II] luminosity of the associated galaxy, which provides an estimate for the star formation rate. With this correlation, the authors were able to show that the star formation rate probed by strong Mg II absorption follows the star formation history up to at least  $z \sim 2$ . Matejek & Simcoe (2012) used similar methods for Mg II absorption in infrared wavelengths with the FIRE spectrograph on Magellan and were able to extend the redshift range out to  $z < 6$ . They found that the star formation rate as probed by Mg II traces the global star formation rate out to  $z < 6$ , including the peak at  $z \sim 2-3$ . Thus, the Mg II equivalent width, and possibly the velocity/column density structure, of the strongest absorbers traces the global star formation rate up to  $z = 6$ .

Additionally, the equivalent width of Mg II absorption has long been found to anti-correlate with impact parameter at up to a  $7.9\sigma$  significance (e.g., Lanzetta & Bowen 1990; Steidel et al. 1994; Kacprzak et al. 2008; Chen et al. 2010; Nielsen et al. 2013a,b), where the equivalent width decreases with increasing impact parameter. More recently, Churchill et al. (2013a) found that  $W_r(2796)$  anti-correlates with the impact parameter normalized by the virial radius of the galaxy,  $D/R_{\text{vir}}$ , at the  $\sim 9\sigma$  level, a more significant anti-correlation than with  $D$  alone. Given that the equivalent width is proportional to the number of clouds (or velocity components) fit with Voigt profile modeling (e.g., Petitjean & Bergeron 1990; Churchill et al. 2003; Evans 2011), this anti-correlation may be due to the column densities, velocity spreads, or both diminishing with projected distance from the galaxy.

These results indicate that examining the kinematic structure and/or column density distribution of the gas traced by Mg II absorption over time and space is critical in understanding the detailed physics of the baryon cycle processes occurring in the CGM. In particular, studying the detailed velocity structure and column density distributions of the absorbers constrains the gas physics involved.

Many works examining the detailed Mg II absorber kinematics have focused on the clustering of VP components in Mg II absorbers by constructing a two-point correlation function (TPCF) for their samples using VP component velocities (Sargent et al. 1988; Petitjean & Bergeron 1990; Churchill 1997; Churchill & Vogt 2001; Churchill et al. 2003; Evans 2011). Churchill et al. (2003) fitted their TPCFs with two Gaussian components, where the narrower component is associated with vertical dispersions in face-on galaxy disks. The second and more broad component may represent the rotational motions in edge-on disks (Churchill et al. 2003). More recently, Evans (2011) required three components to fit their TPCF because their sample was more than an order of magnitude larger than previous works and therefore more sensi-

tive to an extended tail in the distribution. Evans (2011) did not try to interpret their fitted Gaussian components, stating that doing so would be an oversimplification. This is reasonable since their absorber sample spans a large redshift range ( $0.1 < z_{\text{abs}} < 2.6$ ) and likely probes the CGM of a variety of galaxy types.

What these previous absorber kinematics studies lack is the connection between the detailed kinematics of these absorbers to the properties of their host galaxies. In a companion paper (Paper V of the MAGIIICAT series; Nielsen et al. 2015), we examined the kinematics as a function of galaxy color, inclination, and the azimuthal angle at which the CGM is probed. We characterized the kinematics by creating pixel-velocity two-point correlation functions (TPCFs; similar to the TPCFs used in previous works) for various color and orientation subsamples. We found that absorbers hosted by blue galaxies in “face-on” orientations, especially near the projected galaxy minor axis, have the largest velocity dispersions, while absorbers hosted by red galaxies for all orientations have small velocity dispersions. We concluded that for blue galaxies, gas entrained in bipolar outflows may have large velocity dispersions and may be fragmented into clouds with smaller column densities, while gas accreting onto or rotating around the galaxy along the major axis (especially for “edge-on” orientations) may be more coherent, due to larger cloud column densities and smaller velocity dispersions. Conversely, we attributed small velocity dispersions for red galaxies along the minor axis to a lack of outflows, but larger velocity dispersions along the major axis may indicate gas that is accreting onto or rotating around the galaxy.

In this paper, we examine the kinematics of Mg II absorption by using the same pixel-velocity TPCF method as Nielsen et al. (2015), but do so as a function of galaxy rest-frame  $B-K$  color, redshift,  $z_{\text{gal}}$ , and impact parameter normalized by the virial radius,  $D/R_{\text{vir}}$ . We organize this paper as follows. Section 2 details our sample, including both galaxy properties and quasar spectra. Section 3 briefly characterizes quasar absorption line kinematics in terms of Voigt profile components and then details our methods for calculating pixel-velocity two-point velocity correlation functions, presenting only a bivariate analysis of the TPCFs with galaxy rest-frame color,  $B-K$ . Section 4 presents a multivariate analysis in the TPCFs for cuts in galaxy color, redshift, and  $D/R_{\text{vir}}$ . We discuss our results in Section 5, and summarize and conclude our findings in Section 6.

## 2. SAMPLE AND DATA ANALYSIS

### 2.1. Galaxy Properties

All 39 galaxies ( $0.3 < z_{\text{gal}} < 1.0$ ) studied here are a subset of the Mg II Absorber–Galaxy Catalog (MAGIIICAT) and we refer the reader to Paper I of the series (Nielsen et al. 2013b) for full details of the data, the selection methods, and how galaxy properties were determined. To summarize, each galaxy is spectroscopically identified to be located at the redshift of an associated Mg II absorber (whether absorption was detected and measured *a priori* or not) and within a projected distance  $D < 200$  kpc from a background quasar. All galaxies are isolated to the limits of the data available (for details, see Nielsen et al. 2013b), where isolation is defined as having no spectroscopically identified galaxy within 100 kpc (projected) and within a line-of-sight velocity separation of  $500 \text{ km s}^{-1}$ . For each galaxy, we have spectroscopic redshifts,  $z_{\text{gal}}$ , rest-frame  $B$ - and  $K$ -band AB magnitudes and luminosi-

**Table 1**  
Absorber–Galaxy Properties

(1) QSO	(2) J-Name	(3) $z_{\text{gal}}$	(4) $B-K$	(5) $D$ (kpc)	(6) $D/R_{\text{vir}}$	(7) $\log(M_{\text{h}}/M_{\odot})$	(8) $V_{\text{circ}}$ (km s <sup>-1</sup> )	(9) $z_{\text{abs}}$	(10) $W_{\text{r}}(2796)$ (Å)	(11) $\log N(\text{Mg II})$ (cm <sup>-2</sup> )	(12) Ref <sup>a</sup>
0002+051	J000520.21+052411.80	0.298	2.43	59.2	0.31	12.0 <sup>+0.3</sup> <sub>-0.2</sub>	211 <sup>+45</sup> <sub>-26</sub>	0.298059	0.244 ± 0.003	13.14 ± 0.08	1
0002+051	J000520.21+052411.80	0.592	2.05	36.0	0.14	12.3 <sup>+0.2</sup> <sub>-0.2</sub>	291 <sup>+38</sup> <sub>-29</sub>	0.591365	0.102 ± 0.002	12.60 ± 0.11	1
0002+051	J000520.21+052411.80	0.85180	0.74	25.9	0.14	11.8 <sup>+0.2</sup> <sub>-0.2</sub>	220 <sup>+40</sup> <sub>-24</sub>	0.851393	1.089 ± 0.008	14.43 ± 0.24	1
0058+019	J010054.15+021136.52	0.6128	1.32	29.5	0.24	11.4 <sup>+0.4</sup> <sub>-0.2</sub>	151 <sup>+51</sup> <sub>-20</sub>	0.612586	1.684 ± 0.004	15.74 ± 0.12	2
0102-190	J010516.82-184641.9	1.025	...	40.0	0.17	12.1 <sup>+0.1</sup> <sub>-0.1</sub>	284 <sup>+31</sup> <sub>-25</sub>	1.026450	0.946 ± 0.010	15.15 ± 0.45	3
0117+213	J012017.20+213346.00	0.5763	2.09	7.8	0.02	12.9 <sup>+0.1</sup> <sub>-0.1</sub>	415 <sup>+35</sup> <sub>-37</sub>	0.576398	0.902 ± 0.007	~ 15.31 <sup>b</sup>	2
0117+213	J012017.20+213346.00	0.729	2.12	55.4	0.14	12.9 <sup>+0.1</sup> <sub>-0.1</sub>	434 <sup>+33</sup> <sub>-35</sub>	0.729077	0.244 ± 0.005	13.04 ± 0.08	1
0150-202	J015227.32-200107.10	0.780	1.03	54.7	0.26	12.1 <sup>+0.2</sup> <sub>-0.2</sub>	252 <sup>+38</sup> <sub>-27</sub>	0.779796	0.404 ± 0.016	15.80 ± 0.17	3
0229+131	J023145.89+132254.71	0.4167	2.04	36.9	0.14	12.4 <sup>+0.2</sup> <sub>-0.2</sub>	285 <sup>+34</sup> <sub>-29</sub>	0.417338	0.816 ± 0.020	13.83 ± 0.22	1
0235+164	J023838.93+163659.27	0.852	1.48	7.6	0.02	12.6 <sup>+0.1</sup> <sub>-0.1</sub>	370 <sup>+31</sup> <sub>-32</sub>	0.852255	0.505 ± 0.004	13.68 ± 0.12	3
0302-223	J030450.10-221157.00	0.418	...	126.0	0.20	13.5 <sup>+0.1</sup> <sub>-0.1</sub>	625 <sup>+47</sup> <sub>-52</sub>	0.420411	0.727 ± 0.028	14.76 ± 0.96	3
0302-223	J030450.10-221157.00	1.000	...	61.2	0.31	12.0 <sup>+0.2</sup> <sub>-0.1</sub>	248 <sup>+34</sup> <sub>-24</sub>	1.009382	1.099 ± 0.036	15.22 ± 0.50	2
0334-204	J033626.90-201940.00	1.120	...	64.3	0.19	12.6 <sup>+0.1</sup> <sub>-0.1</sub>	404 <sup>+30</sup> <sub>-32</sub>	1.117706	1.706 ± 0.020	16.85 ± 0.30	3
0349-146	J035128.54-142908.71	0.3567	0.28	71.3	0.42	11.9 <sup>+0.3</sup> <sub>-0.2</sub>	193 <sup>+52</sup> <sub>-25</sub>	0.357168	0.175 ± 0.007	13.86 ± 0.30	1
0454-220	J045608.92-215909.40	0.48382	1.66	107.1	0.44	12.3 <sup>+0.2</sup> <sub>-0.2</sub>	270 <sup>+38</sup> <sub>-28</sub>	0.483337	0.426 ± 0.007	13.68 ± 0.39	1
0454+039	J045647.17+040052.94	0.8596	...	16.0	0.14	11.2 <sup>+0.4</sup> <sub>-0.2</sub>	145 <sup>+49</sup> <sub>-19</sub>	0.859569	1.476 ± 0.009	~ 15.51 <sup>b</sup>	2
0827+243	J083052.08+241059.82	0.5247	2.23	37.2	0.15	12.3 <sup>+0.2</sup> <sub>-0.2</sub>	282 <sup>+38</sup> <sub>-29</sub>	0.524966	2.419 ± 0.012	~ 15.19 <sup>b</sup>	1
0836+113	J083933.01+111203.82	0.78682	0.86	26.8	0.15	11.8 <sup>+0.3</sup> <sub>-0.2</sub>	212 <sup>+46</sup> <sub>-24</sub>	0.786725	2.113 ± 0.019	15.54 ± 7.39	1
1019+309	J102230.29+304105.11	0.346	1.23	46.0	0.27	11.9 <sup>+0.3</sup> <sub>-0.2</sub>	193 <sup>+52</sup> <sub>-25</sub>	0.346246	0.628 ± 0.017	15.54 ± 0.41	3
1038+064	J104117.16+061016.92	0.4432	2.81	55.9	0.29	12.0 <sup>+0.3</sup> <sub>-0.2</sub>	221 <sup>+43</sup> <sub>-26</sub>	0.441453	0.673 ± 0.011	13.72 ± 0.26	1
1100-264	J110325.29-264515.7	0.359	...	60.8	0.31	12.0 <sup>+0.3</sup> <sub>-0.2</sub>	216 <sup>+46</sup> <sub>-27</sub>	0.358989	0.545 ± 0.001	14.26 ± 0.08	3
1148+387	J115129.37+382552.35	0.5536	1.19	20.4	0.11	12.0 <sup>+0.3</sup> <sub>-0.2</sub>	224 <sup>+45</sup> <sub>-27</sub>	0.553363	0.640 ± 0.013	13.47 ± 0.13	1
1209+107	J121140.59+103002.02	0.392	1.02	37.5	0.27	11.6 <sup>+0.4</sup> <sub>-0.2</sub>	158 <sup>+58</sup> <sub>-22</sub>	0.392924	1.187 ± 0.005	13.94 ± 0.30	1
1222+228	J122527.39+223513.0	0.5502	2.17	37.7	0.26	11.6 <sup>+0.4</sup> <sub>-0.2</sub>	170 <sup>+54</sup> <sub>-23</sub>	0.550198	0.094 ± 0.009	12.45 ± 0.36	1
1229-021	J123200.01-022405.27	0.7546	1.33	12.4	0.07	11.8 <sup>+0.3</sup> <sub>-0.2</sub>	215 <sup>+43</sup> <sub>-24</sub>	0.756903	0.303 ± 0.003	13.44 ± 0.07	2
1241+176	J124410.82+172104.52	0.550	1.34	21.1	0.12	11.8 <sup>+0.3</sup> <sub>-0.2</sub>	202 <sup>+47</sup> <sub>-25</sub>	0.550482	0.465 ± 0.011	13.63 ± 0.12	1
1246-057	J124913.85-055919.07	0.637	1.63	29.0	0.18	11.7 <sup>+0.3</sup> <sub>-0.2</sub>	192 <sup>+45</sup> <sub>-23</sub>	0.639909	0.450 ± 0.004	13.74 ± 0.26	1
1248+401	J125048.32+395139.48	0.7725	1.28	35.4	0.23	11.6 <sup>+0.3</sup> <sub>-0.2</sub>	185 <sup>+48</sup> <sub>-23</sub>	0.772957	0.695 ± 0.005	13.85 ± 2.32	2
1254+047	J125659.92+042734.39	0.9341	1.22	12.5	0.09	11.6 <sup>+0.3</sup> <sub>-0.2</sub>	184 <sup>+47</sup> <sub>-22</sub>	0.934231	0.338 ± 0.005	13.25 ± 0.10	2
1317+277	J131956.23+272808.22	0.6610	1.45	103.1	0.46	12.1 <sup>+0.2</sup> <sub>-0.2</sub>	259 <sup>+37</sup> <sub>-27</sub>	0.660049	0.320 ± 0.006	13.13 ± 0.43	1
1331+170	J133335.78+164904.01	0.7443	2.02	30.5	0.15	12.0 <sup>+0.2</sup> <sub>-0.2</sub>	245 <sup>+39</sup> <sub>-27</sub>	0.744642	1.836 ± 0.003	14.19 ± 0.10	2
1354+195	J135704.43+191907.37	0.4592	1.40	45.1	0.28	11.7 <sup>+0.3</sup> <sub>-0.2</sub>	184 <sup>+48</sup> <sub>-24</sub>	0.456598	0.773 ± 0.015	13.90 ± 0.92	1
1424-118	J142738.10-120350.00	0.3404	1.77	85.9	0.46	12.0 <sup>+0.3</sup> <sub>-0.2</sub>	209 <sup>+48</sup> <sub>-27</sub>	0.341716	0.100 ± 0.015	12.61 ± 0.06	1
1548+092	J155103.39+090849.25	0.7703	0.68	40.5	0.33	11.4 <sup>+0.4</sup> <sub>-0.2</sub>	155 <sup>+53</sup> <sub>-20</sub>	0.770643	0.229 ± 0.018	13.26 ± 0.02	3
SDSS	J160726.77+471251.37	0.4980	1.41	188.6	0.75	12.3 <sup>+0.2</sup> <sub>-0.2</sub>	281 <sup>+38</sup> <sub>-28</sub>	0.497479	1.237 ± 0.037	15.90 ± 3.53	3
1622+238	J162439.08+234512.20	0.3181	2.85	54.4	0.28	12.0 <sup>+0.3</sup> <sub>-0.2</sub>	215 <sup>+45</sup> <sub>-26</sub>	0.317597	0.491 ± 0.010	13.88 ± 1.17	1
1622+238	J162439.08+234512.20	0.4720	0.92	34.0	0.28	11.4 <sup>+0.5</sup> <sub>-0.2</sub>	142 <sup>+54</sup> <sub>-19</sub>	0.471930	0.769 ± 0.006	14.48 ± 2.16	1
1622+238	J162439.08+234512.20	0.6560	0.93	99.3	0.69	11.6 <sup>+0.4</sup> <sub>-0.2</sub>	173 <sup>+48</sup> <sub>-22</sub>	0.656106	1.446 ± 0.006	~ 14.82 <sup>b</sup>	1
1622+238	J162439.08+234512.20	0.7975	1.66	71.3	0.35	12.0 <sup>+0.2</sup> <sub>-0.2</sub>	247 <sup>+40</sup> <sub>-27</sub>	0.797078	0.468 ± 0.008	13.28 ± 0.06	1
1622+238	J162439.08+234512.20	0.8909	0.41	23.2	0.14	11.7 <sup>+0.3</sup> <sub>-0.2</sub>	201 <sup>+43</sup> <sub>-24</sub>	0.891276	1.548 ± 0.004	~ 14.90 <sup>b</sup>	1
2128-123	J213135.26-120704.79	0.430	2.06	48.1	0.24	12.0 <sup>+0.2</sup> <sub>-0.2</sub>	225 <sup>+43</sup> <sub>-26</sub>	0.429812	0.452 ± 0.008	~ 14.18 <sup>b</sup>	2
2145+067	J214805.45+065738.60	0.790	1.39	40.8	0.19	12.1 <sup>+0.2</sup> <sub>-0.2</sub>	256 <sup>+39</sup> <sub>-27</sub>	0.790866	0.547 ± 0.005	13.42 ± 0.62	2
2206-199	J220852.07-194359.0	0.752	...	11.7	0.06	11.9 <sup>+0.3</sup> <sub>-0.2</sub>	221 <sup>+43</sup> <sub>-25</sub>	0.751923	0.890 ± 0.002	16.23 ± 0.04	2
2206-199	J220852.07-194359.0	0.948	0.74	86.9	0.37	12.2 <sup>+0.2</sup> <sub>-0.1</sub>	286 <sup>+35</sup> <sub>-27</sub>	0.948362	0.256 ± 0.003	13.18 ± 0.07	2
2206-199	J220852.07-194359.0	1.01655	0.63	104.4	0.31	12.6 <sup>+0.1</sup> <sub>-0.1</sub>	399 <sup>+30</sup> <sub>-32</sub>	1.017050	1.058 ± 0.004	14.43 ± 0.11	2
2231-002	J223408.99+000001.69	0.8549	...	23.6	0.16	11.6 <sup>+0.3</sup> <sub>-0.2</sub>	184 <sup>+45</sup> <sub>-22</sub>	0.855069	0.784 ± 0.004	13.75 ± 0.13	2
2343+125	J234628.21+124859.9	0.7313	1.22	32.5	0.26	11.4 <sup>+0.4</sup> <sub>-0.2</sub>	154 <sup>+53</sup> <sub>-20</sub>	0.731219	1.655 ± 0.006	~ 16.21 <sup>b</sup>	2

<sup>a</sup> Mg II Absorption Measurements: (1) [Kacprzak et al. \(2011\)](#), (2) [Evans \(2011\)](#), and (3) This work.

<sup>b</sup> At least one cloud is not well constrained, resulting in a large uncertainty.



ties, rest-frame  $B-K$  colors, and quasar–galaxy impact parameters,  $D$ . We also have halo masses,  $\log(M_h/M_\odot)$ , virial radii,  $R_{\text{vir}}$ , and maximum circular velocities,  $V_{\text{circ}}$ , from halo abundance matching, the details for which are presented in Paper III (Churchill et al. 2013b).

While the data for the absorber–galaxy pairs used here are published elsewhere (Kacprzak et al. 2011; Evans 2011; Nielsen et al. 2013b; Churchill et al. 2013b), we present the galaxy and absorber data for each pair in Table 1. Columns (1) and (2) are the quasar field names, columns (3)–(8) are the galaxy properties and columns (9)–(12) are the absorber properties. Columns (3)–(5) were published in Nielsen et al. (2013b), while columns (7) and (8) and the  $R_{\text{vir}}$  values for column (6) were published in Churchill et al. (2013b).

In order to investigate any dependencies of MgII absorption on the star formation rate over time, as well as any radial dependencies, we slice our sample into various subsamples based on median galaxy rest-frame color,  $B-K^1$ , redshift,  $z_{\text{gal}}$ , and impact parameter normalized by the virial radius,  $D/R_{\text{vir}}$ . The median value is appropriate here as it allows for roughly equal sample sizes for comparison. A summary is presented in Table 2, which details the median value(s) by which the subsamples are defined and the number of galaxies in each subsample. The table also lists the median  $z_{\text{gal}}$  and  $D/R_{\text{vir}}$  for each subsample after the full sample cuts are made.

We note that, though the focus of this paper is on galaxy  $B-K$  colors, it is difficult to disentangle effects due to color from those due to galaxy halo masses,  $\log(M_h/M_\odot)$ . A Kendall- $\tau$  rank correlation test on color and mass results in a  $2.8\sigma$  correlation such that redder galaxies tend to be more massive. Figure 1 presents  $B-K$  versus  $\log(M_h/M_\odot)$  with points colored by  $z_{\text{gal}}$ . Dashed lines indicate the median color and mass of the sample. Almost all galaxies in our sample lie within the blue, low mass or red, high mass regions of Figure 1, with the exception of four blue, high mass galaxies and four red, low mass galaxies. If we instead conduct our analysis with  $\log(M_h/M_\odot)$ , we find no significant differences in the TPCFs when we compare blue samples to low mass samples or red to high mass samples. Therefore, any differences we find in the TPCFs is due to a color–mass dependence rather than just a color dependence. To mitigate this, we account for the host galaxy mass by normalizing velocities by the maximum circular velocity,  $V_{\text{circ}}$ , of the host galaxy.

We also examine possible trends between the properties we use to cut the sample to rule out the possibility that any differences we may find between subsamples are mainly due to biases in the data. We ran a Kendall- $\tau$  rank correlation test between  $B-K$  and  $z_{\text{gal}}$  and find an anti-correlation with a significance of  $3.1\sigma$ . In this case, bluer galaxies tend to be located at higher redshift, as can be seen in Figure 1. Comparing  $B-K$  and  $D/R_{\text{vir}}$  results in an insignificant anti-correlation at  $0.8\sigma$ , while we also find an insignificant anti-correlation between  $z_{\text{gal}}$  and  $D/R_{\text{vir}}$  at  $2.0\sigma$ .

## 2.2. Quasar Spectra

The sample we present here is a MgII absorption-selected sample. For each of the 39 isolated galaxies, we have a high-resolution spectrum of a nearby background quasar in which absorption is detected at the redshift of the galaxy. Quasar

<sup>1</sup> This ensures the largest and (nearly) equal subsample sizes for comparison rather than cutting by the more traditional galaxy color bimodality (roughly 1.87 for this sample), which would result in small red subsamples and unequal subsample sizes.

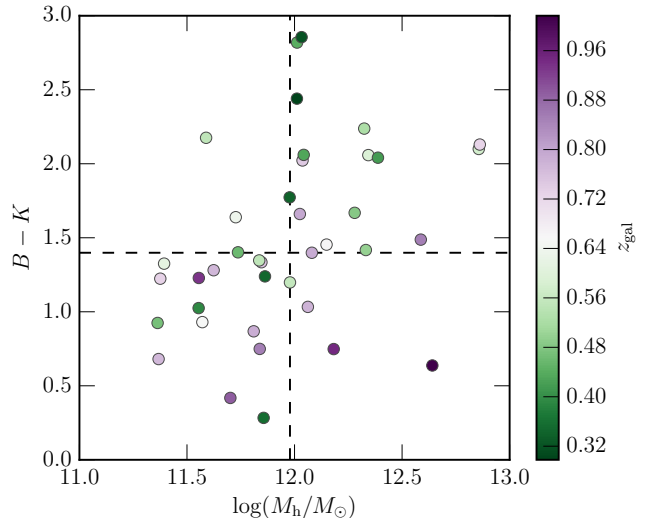


**Figure 1.** Galaxy rest-frame  $B-K$  color versus halo mass,  $\log(M_h/M_\odot)$ . Point colors indicate the galaxy redshift,  $z_{\text{gal}}$ , where the median redshift of ( $z_{\text{gal}} = 0.656$ ) roughly corresponds to the white portion of the color bar. The vertical dashed line represents the median  $\log(M_h/M_\odot)$  of the sample and the horizontal dashed line is the median  $B-K$ . A Kendall- $\tau$  rank correlation test comparing  $B-K$  to  $\log(M_h/M_\odot)$  found a correlation with a significance of  $2.8\sigma$ . This is represented as having most points located in the blue, low mass or red, high mass subsamples.

spectra were observed with HIRES/Keck (Vogt et al. 1994) or UVES/VLT (Dekker et al. 2000). Most spectra and details of their reduction are published in Churchill (1997), Churchill & Vogt (2001), Evans (2011), and/or Kacprzak et al. (2011). We obtained two additional reduced HIRES/Keck spectra through private communication with C. C Steidel and J.-R. Gauthier. These latter two spectra were reduced using the Mauna Kea Echelle Extraction (MAKEE<sup>2</sup>) package.

Full explanations of how the MgII absorption systems are identified in the quasar spectra and Voigt profile fitted are presented in great detail in Churchill (1997), Churchill & Vogt (2001), Churchill et al. (2003), Evans (2011), and Kacprzak et al. (2011). We present only a summary of the process here.

Using SYSANAL (Churchill 1997; Churchill & Vogt 2001; Evans 2011), we detect the MgII  $\lambda\lambda 2796, 2803$  absorption doublet in each spectrum with a  $5\sigma$  ( $3\sigma$ ) significance criterion in the equivalent width spectrum for the  $\lambda 2796$  ( $\lambda 2803$ ) line by following the formalism of Schneider et al. (1993). SYSANAL determines velocity or wavelength bounds that define regions in which absorption is formally detected (“kinematic subsystems”) and calculates the rest-frame equivalent width,  $W_\lambda(2796)$ . The code also defines the absorption redshift,  $z_{\text{abs}}$ , as the median velocity of the apparent optical depth distribution of MgII absorption (Churchill 1997). In Figures 2(a) and (b), we present an example spectrum of quasar Q0235+164 with three MgII kinematic subsystems at  $z_{\text{abs}} = 0.852$ . The black histogram is the spectrum for the MgII  $\lambda 2796$  line (panel (a)) and for the MgII  $\lambda 2803$  line (panel (b)). The shaded regions in panel (a) designate two of the three kinematic subsystems for this system. For our TPCF analysis, we use only the pixels inside these shaded regions.

We then fit all MgII systems using Voigt profile (VP) decomposition with MINFIT (Churchill 1997; Churchill & Vogt 2001; Churchill et al. 2003) and adopt the model with the

<sup>2</sup> <http://www.astro.caltech.edu/~tb/makee/>

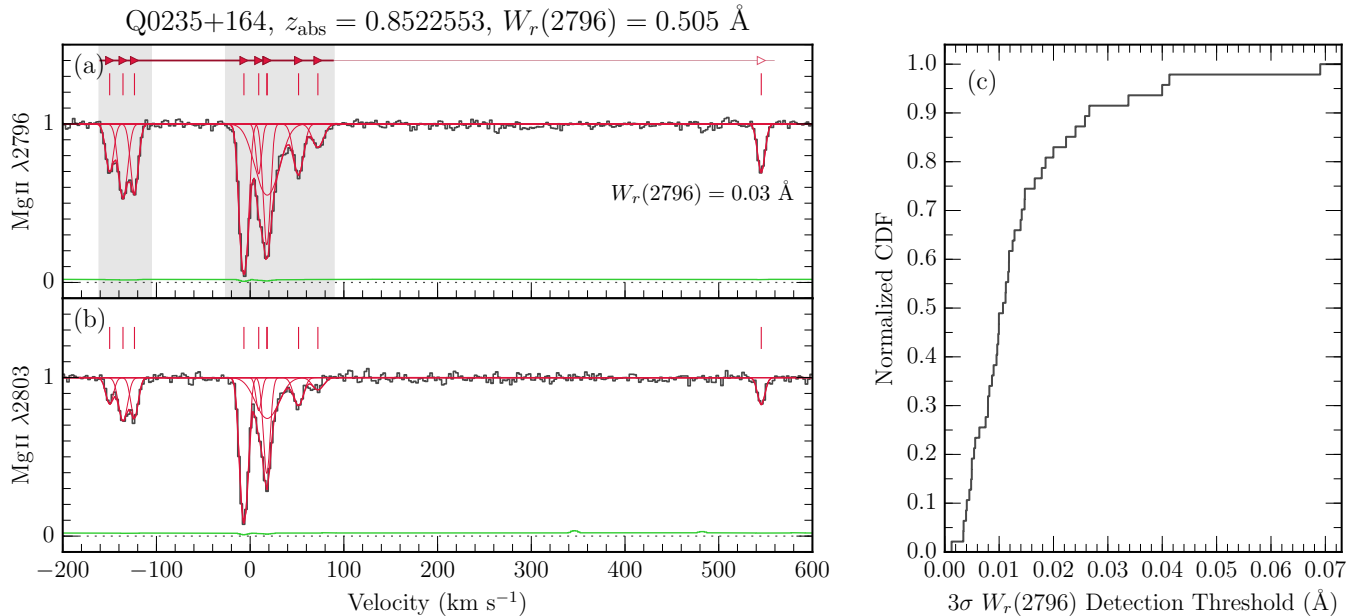


**Figure 2.** An example quasar spectrum focused on the Mg II  $\lambda\lambda 2796, 2803$  absorption doublet in panels (a) and (b). Black histograms are the data, thick red lines are the full Voigt profile fit to the data, and thin red lines are the individual Voigt profile components that compose the total fit. The VP components are centered on the vertical ticks at the top of each panel. The shaded regions indicate the pixels used in the TPCF analysis. The horizontal line and triangles at the top of panel (a) represent a simplified spectrum for use in Figures 3 and 4(a). (c) Cumulative distribution function of the equivalent width detection threshold for the full kinematics sample. This sample is complete to  $\sim 95\%$  at  $0.04 \text{ \AA}$ . We do not include any kinematic subsystems for which  $W_r(2796) < 0.04 \text{ \AA}$ . An example subsystem below this limit is shown at  $v \sim 550 \text{ km s}^{-1}$  in panel (a), which has  $W_r(2796) = 0.03 \text{ \AA}$ .

fewest statistically significant VP components. MINFIT defines the VP component (cloud) velocities, column densities, and Doppler  $b$  parameters. Full details of MINFIT and the fitting process are described in Evans (2011) and most VP fits are presented in Kacprzak et al. (2011). An example VP fit is presented in Figures 2(a) and (b) as the thick red line. Individual VP components are plotted as thin red lines centered at velocities indicated by the red, vertical ticks. This system was fitted with three components in the first shaded region, six in the second shaded region, and one component at larger velocities.

The absorber data are listed in columns (9)–(12) of Table 1<sup>3</sup>. The total column densities,  $\log N(\text{Mg II})$ , in column (11) are calculated by summing the column densities of each cloud. For a few absorbers, at least one cloud in the absorber does not have a well constrained column density. In these cases, we report only the approximate column densities. Column (12) lists the reference for the absorption data. In several instances, we fit the absorbers for this work.

To account for differences in the quality of our spectra and to ensure we can uniformly detect absorption throughout our sample, we use an equivalent width detection threshold. We calculate the mean  $3\sigma W_r(2796)$  detection threshold in each spectrum, defined as the minimum  $W_r(2796)$  a kinematic subsystem should have in order to be detected. Figure 2(c) presents the cumulative distribution function of the detection threshold in each spectrum in our sample, which is  $\sim 95\%$  complete to roughly  $0.04 \text{ \AA}$  within  $\pm 800 \text{ km s}^{-1}$  for all absorbers in our sample. We adopt this value as our equivalent width detection threshold and do not include any kinematic

subsystems with  $W_r(2796) < 0.04 \text{ \AA}$  in our analysis. An example kinematic subsystem that is just below our sensitivity limit with  $W_r(2796) = 0.03 \text{ \AA}$  is presented in Figure 2(a) at  $v \sim 550 \text{ km s}^{-1}$ .

We also have an additional 23 absorber–galaxy pairs with HIRES/Keck or UVES/VLT quasar spectra in which only an upper limit on the Mg II equivalent width was measured, though we do not use the data in this work as we cannot obtain kinematics information for these “nonabsorbers.” In all but one case, the upper limits on absorption are lower than our adopted equivalent width detection threshold. Therefore, if we were able to obtain kinematic information for these systems, they would not be included in our sample as their equivalent widths are too low.

### 3. CHARACTERIZING KINEMATICS

Several methods to examine the kinematics of Mg II absorbers have been used in the literature; two common methods utilize the velocity distribution and/or clustering of VP components. These include the distributions of Voigt profile components and the two-point correlation function.

#### 3.1. Voigt Profile Component Distributions

In Figure 3, we present the kinematics of our Mg II absorbers as a function of rest equivalent width,  $W_r(2796)$ , for all 39 absorber–galaxy pairs, including an additional eight pairs for which we have a high-resolution quasar spectrum but no measured  $B-K$  value. We show a simplified spectrum of each Mg II absorber with a velocity zero point at  $z_{\text{abs}}$ , defined as the optical depth weighted median of the absorption. Clouds (VP components) are plotted as points centered at their fitted line-of-sight velocity (see Figure 2(a)) and total  $W_r(2796)$  of the associated absorber. The spread in velocity of the absorbers is plotted as vertical lines and represents only the largest de-

<sup>3</sup> We have data for two additional MAGIIICAT absorber–galaxy pairs but do not include them in the table nor the analysis. The first is an outlier with  $W_r(2796) = 4.422 \text{ \AA}$  and has no galaxy  $B-K$ . The second has  $W_r(2796) = 0.032 \text{ \AA}$ , which is lower than our detection threshold.

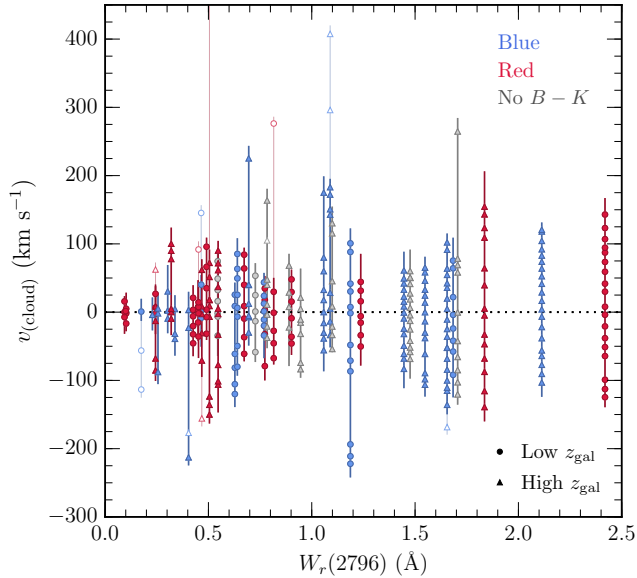


**Figure 3.** Absorber velocity distribution as a function of rest equivalent width,  $W_r(2796)$ . Points represent each individual fitted cloud while vertical lines show the extremes in velocity of each profile, neglecting gaps between kinematic subsystems. Open points and lightly colored lines represent those subsystems which have been dropped from the sample due to our equivalent width detection sensitivity cut ( $W_r(2796) \geq 0.04 \text{ \AA}$ ). See the top of Figure 2(a) for an example to translate points and vertical lines to a spectrum. Point colors and types represent our  $B-K$  and  $z_{\text{gal}}$  subsamples, respectively. The point going off the panel at  $W_r(2796) \sim 0.5 \text{ \AA}$  is a cloud located at  $v_{\text{cloud}} \sim 550 \text{ km s}^{-1}$  and belongs to the absorber presented in Figure 2. Large velocity spreads can be found for nearly the full  $W_r(2796)$  range.

viations from  $z_{\text{abs}}$ ; gaps between kinematic subsystems (i.e., stretches of continuum within the extreme velocity bounds of the absorber) are not presented here. Kinematic subsystems whose equivalent widths are below our sensitivity cut are plotted as open points with lighter vertical lines. Point colors indicate the rest-frame  $B-K$  color of the host galaxy (a proxy for star formation rate), with blue points representing galaxies with  $B-K < 1.4$ , red points as galaxies with  $B-K \geq 1.4$ , and gray points are those galaxies for which we do not have a  $B-K$  measurement (8 galaxies). Point types indicate whether the host galaxy is located at low redshift (circles,  $z_{\text{gal}} < 0.656$ ), or high redshift (triangles,  $z_{\text{gal}} \geq 0.656$ ).

As shown in Figure 3, large absorber velocity spreads can be found for absorbers of nearly all equivalent width strengths, especially when an equivalent width detection threshold is not enforced (open points). The narrowing of the profiles near  $W_r(2796) \sim 1.0-1.2 \text{ \AA}$  is due to the absorbers becoming saturated, which occurs for  $\log N(\text{Mg II}) \sim 13$ . Below this point, large velocity spreads are largely due to several kinematic subsystems spread out in velocity and may have stretches of continuum between subsystems. This is most obvious in the absorber presented in Figure 2(a), which, when including kinematic subsystems below our detection threshold, has the largest velocity spread in the sample. Above this point the number of clouds fit to the profile increases and corresponds to an increasing velocity width. The degeneracy between velocity spread and equivalent width in this plot shows that equivalent width is a poor indicator of absorber kinematics.

We present the kinematics of our Mg II absorbers as a function of galaxy rest-frame  $B-K$  color, redshift,  $z_{\text{gal}}$ , and im-

pact parameter,  $D$ , in Figure 4(a). Point colors and types, along with line colors are similar to those in Figure 3. We find several qualitative trends in these results. Clouds are mostly found within  $|v_{\text{cloud}}| = 150 \text{ km s}^{-1}$  of the absorber systemic velocity. As absorption is probed further from the galaxy (moving outward with increasing  $D$ ), the velocity spread of absorption may decrease from large velocity spreads at low  $D$  to smaller velocity spreads at higher  $D$ . The absorbers may be more extended in velocity for blue galaxies than red. Also, it appears that most of the highest velocity clouds are located around galaxies at high redshift.

This method of examining the absorption kinematics has been used often, though with the velocities shifted to the galaxy systemic velocity (see e.g., Tumlinson et al. 2013; Werk et al. 2013; Mathes et al. 2014). Though the method is effective, it is difficult to extract clear kinematic trends with, for example, galaxy redshift and color, let alone characterizing the kinematics of the gas itself (rather than with respect to the galaxy).

### 3.2. Pixel-velocity Two-point Correlation Functions

We extend beyond the line of work with cloud velocities started by Petitjean & Bergeron (1990) by examining the pixel-velocity two-point correlation function (TPCF) for various galaxy subsamples and compare the resultant line-of-sight velocity dispersions. Previous works constructed TPCFs using cloud (VP component; the ticks at the top of Figure 2(a)) velocities, while we use the velocities of pixels in regions of the spectrum which contribute to the overall Mg II equivalent width (i.e., kinematic subsystems, see shaded regions in Figure 2 for examples). Compared to cloud velocities, pixel velocities better represent the spread in absorption, provide more velocity pairs for better statistics, and can be compared more easily to simulations because the absorption profiles do not need to be Voigt profile modeled. They are also model-independent, i.e., they do not depend on the fitting method used and the resulting fit. We study the velocity dispersions of the absorbers for various galaxy subsamples using the pixel-velocity TPCF.

To first construct the TPCF, which is a measure of the internal absorber velocity dispersion, we define a subsample of galaxies. From the spectra of background quasars associated with these galaxies, we obtain the velocities (where  $v = 0 \text{ km s}^{-1}$  represents  $z_{\text{abs}}$ , the optical depth weighted median of absorption) of pixels located in regions in which Mg II absorption has been formally detected, also known as kinematic subsystems (gray shaded regions of Figure 2(a)). The velocity bounds of these regions are defined by searching the spectrum redwards and bluewards from the subsystem velocity centroid until the significance in the per pixel equivalent width drops below  $1\sigma$  (Churchill & Vogt 2001).

We then combine the pixel velocities from each absorber-galaxy pair in the subsample. This method uses the experiment in which combining a single absorbing sightline around multiple galaxies for a certain subsample is equivalent to multiple absorbing sightlines around a single galaxy of the same type as the subsample. This allows for more robust statistics and prevents any possible bias that might arise from the absorbers with the most pixels. Then the absolute value of the velocity separations is calculated between each possible pixel velocity pair for the subsample to get  $\Delta v_{\text{pixel}}$ . The TPCF is created by binning the velocity separations and normalizing the value in each bin by the total number of pixel velocity

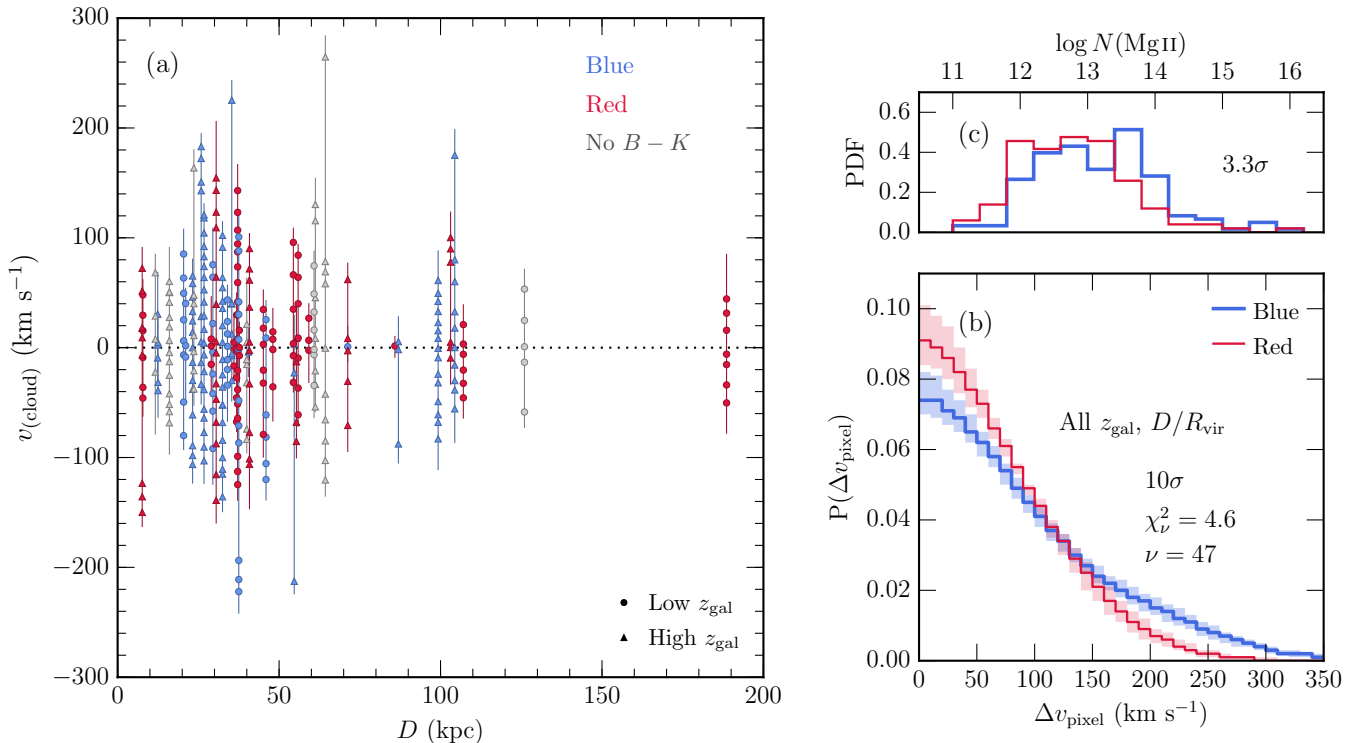


**Figure 4.** (a) Velocity distribution of clouds (Voigt profile components) in the absorption profiles as a function of impact parameter. Points and lines are similar to Figure 3. Most absorption is found within  $|v_{(\text{cloud})}| = 150 \text{ km s}^{-1}$  of  $z_{\text{abs}}$  (which defines the velocity zero point from the optical depth weighted median of absorption) and absorbers located at smaller impact parameters appear to have broader profiles in velocity space than those further away. (b) Pixel-velocity two-point correlation functions for blue and red galaxies (solid lines). Shaded regions represent the  $1\sigma$  uncertainties around the data from a bootstrap analysis. The significance of a chi-squared test comparing the distributions of the blue and red TPCFs is listed in the panel. We find that blue galaxies have larger velocity dispersions than red galaxies. (c) Cloud column density distributions for blue and red galaxies. The counts in each bin have been normalized by the total number of clouds for the subsample. The results of a KS test comparing the plotted subsamples is listed in the panel. Blue galaxies tend to have larger column densities than red galaxies at the  $3.3\sigma$  level.

pairs in the subsample to account for differing numbers of pixels in each subsample when comparing between subsamples. The TPCF is therefore a probability distribution function. We use a bin size of  $10 \text{ km s}^{-1}$ , which corresponds to roughly one resolution element of both the HIRES/Keck and UVES/VLT spectrographs (three pixels per resolution element, with a FWHM resolution of  $\sim 6.6 \text{ km s}^{-1}$ ).

To determine the uncertainties on the TPCFs, we conduct a bootstrap analysis. We randomly draw with replacement a sample of kinematic subsystems from the subsample we are examining which contains the same number of kinematic subsystems as the original data and construct a TPCF. We run 1000 bootstrap realizations and then calculate the  $1\sigma$  standard deviations from the mean of the realizations in each TPCF bin. The bootstrap uncertainties are plotted as shaded regions around the TPCF.

We also characterize the TPCFs by measuring the velocity separations within which 50% and 90% of the data reside,  $\Delta v(50)$  and  $\Delta v(90)$ , respectively. For these TPCFs,  $v$  in  $\Delta v(50)$  and  $\Delta v(90)$  represents  $v_{\text{pixel}}$ . Uncertainties on these values are obtained from the bootstrap analysis and represent  $1\sigma$  deviations from the mean. These values and their uncertainties are presented in Table 2 for each subsample.

We present the absorber TPCFs comparing blue and red galaxies in Figure 4(b). Blue galaxies are presented as the thick blue line with blue shaded areas indicating the bootstrap uncertainties, while the thin red line and shading represents red galaxies. In this panel, we find that the absorption as-

sociated with blue galaxies has a larger velocity dispersion than with red galaxies, which can also be seen in panel (a). To test whether the two samples were drawn from the same population, we ran a chi-squared test on the binned TPCFs (including the uncertainties on the TPCF) and find that the null hypothesis that the samples were drawn from the same population can be ruled out at the  $10\sigma$  level. The significance,  $\sigma$ , the reduced chi-squared,  $\chi^2_{\nu}$ , and the number of degrees of freedom,  $\nu$ , is presented in Figure 4(b). We find that both the  $\Delta v(50)$  and  $\Delta v(90)$  measurements for blue galaxies ( $75 \text{ km s}^{-1}$  and  $205 \text{ km s}^{-1}$ , respectively) are greater than for red galaxies ( $60 \text{ km s}^{-1}$  and  $151 \text{ km s}^{-1}$ , respectively). This indicates that absorbers around blue galaxies have significantly larger velocity dispersions than those around red galaxies.

### 3.3. Cloud Column Densities

Examining the cloud column densities in addition to the absorption velocity dispersions yields a more complete picture of the physics involved in placing and maintaining MgII absorption in the halos of galaxies. This is especially true considering that column densities depend on the ionization conditions, temperature, metallicity, and path length of the gas that is being probed. As stated in Section 2.2, we obtain cloud column densities for absorbers using Voigt profile decomposition. We examine the column density distributions for the same subsamples we use for the TPCFs in order to obtain a more complete picture of the gas properties as a function of galaxy properties, and therefore, evolutionary processes.



**Table 2**  
TPCF  $\Delta v(50)$  and  $\Delta v(90)$  Measurements

Sample	Cut	Cut	$\langle z_{\text{gal}} \rangle$	$\langle D/R_{\text{vir}} \rangle$	# Gals	$\Delta v_{\text{pixel}}$		$\Delta(v_{\text{pixel}}/V_{\text{circ}})$	
						$\Delta v(50)^a$	$\Delta v(90)^a$	$\Delta v(50)$	$\Delta v(90)$
Figure 4(b) and Figure 5									
Blue	$B-K < 1.4$	...	0.754	0.26	19	$75^{+5}_{-6}$	$205^{+12}_{-17}$	$0.63^{+0.06}_{-0.07}$	$1.76^{+0.15}_{-0.18}$
Red	$B-K \geq 1.4$	...	0.537	0.25	20	$60^{+5}_{-6}$	$151^{+11}_{-14}$	$0.35^{+0.03}_{-0.04}$	$0.87^{+0.07}_{-0.09}$
Figure 6 and Figure 7									
Blue – Low $z_{\text{gal}}$	$B-K < 1.4$	$z_{\text{gal}} < 0.656$	0.472	0.27	7	$78^{+9}_{-13}$	$199^{+21}_{-35}$	$0.70^{+0.10}_{-0.14}$	$1.84^{+0.23}_{-0.36}$
Blue – High $z_{\text{gal}}$	$B-K < 1.4$	$z_{\text{gal}} \geq 0.656$	0.783	0.25	12	$71^{+4}_{-6}$	$200^{+11}_{-15}$	$0.58^{+0.05}_{-0.07}$	$1.61^{+0.14}_{-0.16}$
Red – Low $z_{\text{gal}}$	$B-K \geq 1.4$	$z_{\text{gal}} < 0.656$	0.472	0.27	14	$49^{+7}_{-8}$	$123^{+16}_{-23}$	$0.29^{+0.04}_{-0.05}$	$0.73^{+0.07}_{-0.11}$
Red – High $z_{\text{gal}}$	$B-K \geq 1.4$	$z_{\text{gal}} \geq 0.656$	0.767	0.17	6	$73^{+6}_{-7}$	$177^{+13}_{-15}$	$0.41^{+0.04}_{-0.05}$	$1.00^{+0.10}_{-0.12}$
Figure 8 and Figure 9									
Blue – Low $D/R_{\text{vir}}$	$B-K < 1.4$	$D/R_{\text{vir}} < 0.24$	0.780	0.13	9	$68^{+5}_{-8}$	$193^{+14}_{-19}$	$0.58^{+0.04}_{-0.06}$	$1.59^{+0.15}_{-0.16}$
Blue – High $D/R_{\text{vir}}$	$B-K < 1.4$	$D/R_{\text{vir}} \geq 0.24$	0.656	0.28	10	$77^{+6}_{-9}$	$199^{+15}_{-22}$	$0.67^{+0.09}_{-0.11}$	$1.76^{+0.20}_{-0.28}$
Red – Low $D/R_{\text{vir}}$	$B-K \geq 1.4$	$D/R_{\text{vir}} < 0.24$	0.637	0.14	10	$72^{+7}_{-9}$	$174^{+14}_{-16}$	$0.37^{+0.05}_{-0.07}$	$0.95^{+0.11}_{-0.14}$
Red – High $D/R_{\text{vir}}$	$B-K \geq 1.4$	$D/R_{\text{vir}} \geq 0.24$	0.459	0.31	10	$48^{+2}_{-3}$	$114^{+4}_{-7}$	$0.31^{+0.02}_{-0.03}$	$0.75^{+0.04}_{-0.06}$

<sup>a</sup> km s<sup>-1</sup>

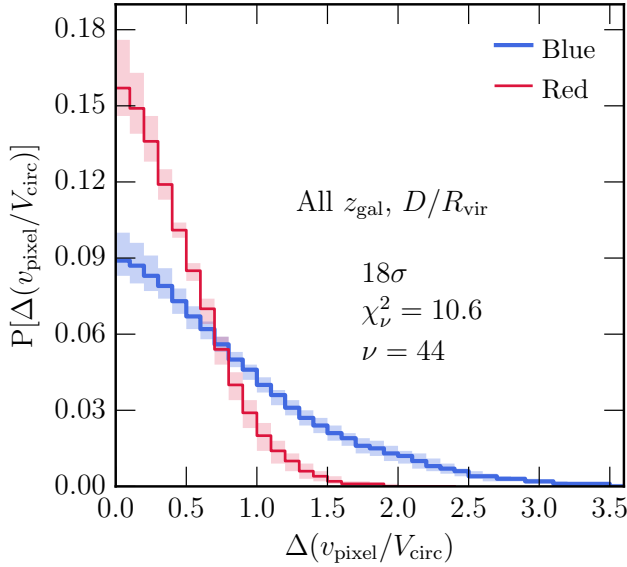


**Figure 5.** Pixel-velocity TPCFs normalized by the host galaxy circular velocity (to account for galaxy halo mass) for blue and red galaxies. Normalizing the velocities by  $V_{\text{circ}}$  does not change the general result that absorbers around blue galaxies have larger velocity dispersions than around red galaxies, which was also presented in Figure 4(b). However, the result becomes more significant at the  $18\sigma$  level.

In Figure 4(c), we present the cloud column density distributions for blue and red galaxy subsamples. The counts in each column density bin are normalized to the total number of clouds in each subsample to create a probability distribution function. We use the Kolmogorov–Smirnov (KS) test comparing the plotted column density distributions to determine if the two samples were drawn from the same population. With a  $3.3\sigma$  significance, we find that the null hypothesis that the

cloud column densities for blue and red galaxies were drawn from the same population can be ruled out. Thus, absorption associated with blue galaxies tends to have larger column densities than absorption associated with red galaxies.

### 3.4. Mass-normalized Pixel-velocity TPCF

To account for the mass of the galaxy hosting absorption, we normalize the pixel velocities by the maximum circular velocity,  $V_{\text{circ}}$ , of the host galaxy. We do this because our sample spans a range of galaxy halo masses and because of the fact that our red galaxies tend to be more massive than our blue galaxies (see section 2 and Figure 1). Here we present methods for constructing normalized absorber TPCFs.

We calculate the mass-normalized absorber TPCF using a similar procedure as the unnormalized absorber TPCF. Before we calculate the pixel pair velocity separations for a given subsample, we normalize each pixel velocity by the  $V_{\text{circ}}$  of the host galaxy. After determining the velocity separations,  $\Delta(v_{\text{pixel}}/V_{\text{circ}})$ , we bin the values using the same methods used for the unnormalized TPCFs. The normalized absorber TPCF for blue and red galaxies is presented in Figure 5. The general result in this panel that blue galaxies have a larger absorber velocity dispersion than red galaxies does not differ from the unnormalized absorber TPCF in Figure 4(b), but the significance of the chi-squared test is greater here. We also present measurements of  $\Delta v(50)$  and  $\Delta v(90)$  for each subsample in the right-most columns of Table 2, where the  $\nu$  in this case represents  $(v_{\text{pixel}}/V_{\text{circ}})$ . For these subsamples, we find that the values of  $\Delta v(50)$  and  $\Delta v(90)$  are very different, with much larger values for the blue subsample (0.6 and 1.8, respectively) than the red subsample (0.35 and 0.9, respectively); the values for the blue subsample are roughly twice as large as for the red subsample.

## 4. MULTIVARIATE ANALYSIS



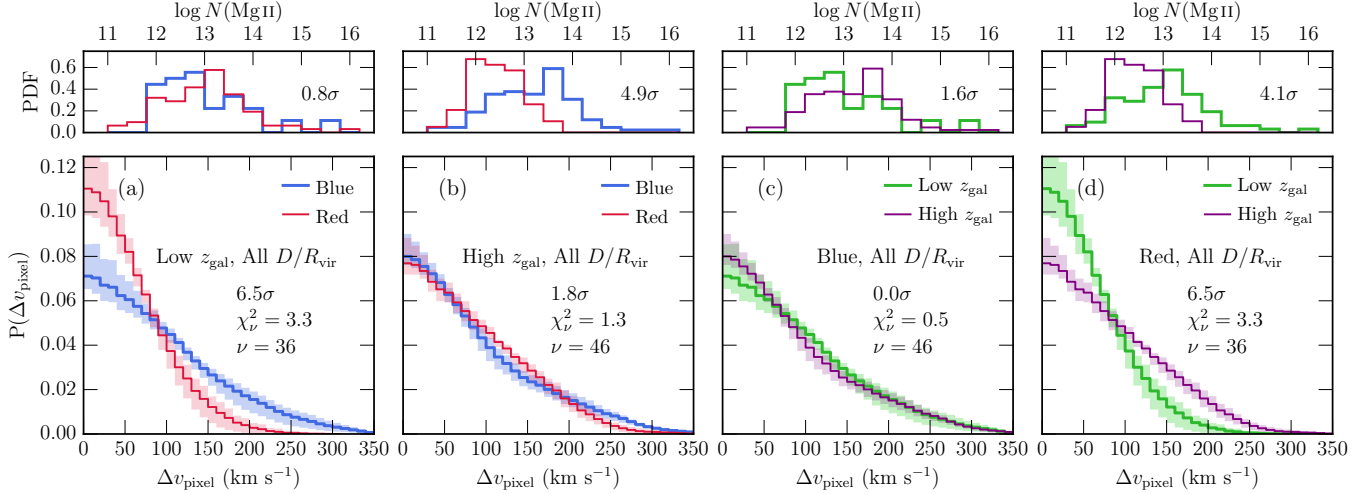


**Figure 6.** Pixel-velocity two-point correlation functions for color and redshift subsamples in the bottom panels. Solid lines are the TPCFs while shaded regions are the  $1\sigma$  bootstrap uncertainties. We list the significance, the reduced chi-squared value,  $\chi^2_\nu$ , and the degrees of freedom,  $\nu$ , from a chi-squared test comparing subsamples in each panel. In each case, blue galaxies have  $B-K < 1.4$  and red galaxies have  $B-K \geq 1.4$ . We find that red, low  $z_{\text{gal}}$  ( $z_{\text{gal}} < 0.656$ ) galaxies have significantly smaller absorber velocity dispersions than red, high  $z_{\text{gal}}$  ( $z_{\text{gal}} \geq 0.656$ ) galaxies or blue galaxies (panels (d) and (a)), whereas there are no differences in the velocity dispersions for blue galaxies (panel (c)) or for blue and red galaxies at high  $z_{\text{gal}}$  (panel (b)). The panels above the TPCFs present the cloud column density distributions for the same TPCF subsamples. The plotted significance in each panel is the result of a KS test between subsamples. The column densities only differ with redshift for red galaxies, with smaller column densities at higher redshifts.

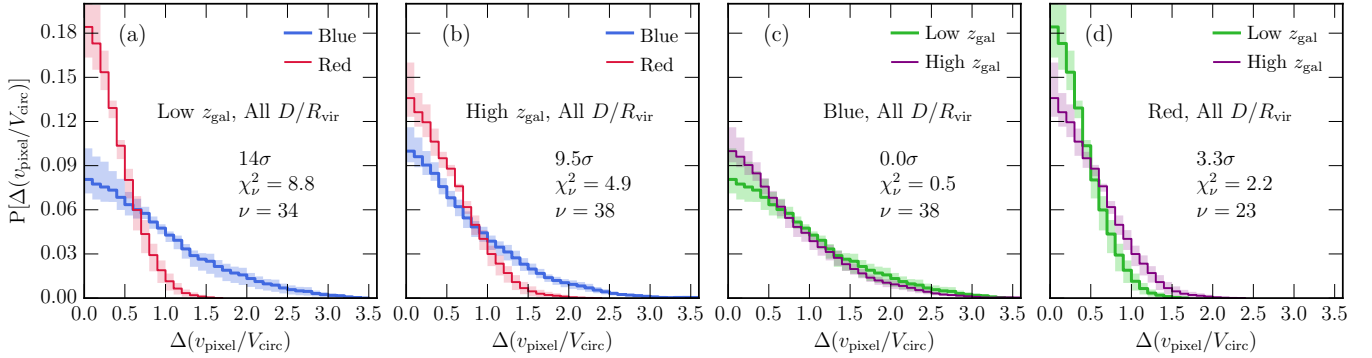


**Figure 7.** Mass-normalized TPCFs for the same color and redshift subsamples as those in Figure 6. Normalizing the velocities by  $V_{\text{circ}}$  does not change the general results compared to those presented in Figure 6, with the exception of the high redshift samples in panel (b). In this panel, we find that blue galaxies have a larger absorber velocity dispersion than red galaxies, in contrast to no difference for the unnormalized TPCFs. The redshift evolution of red galaxies in panel (d) becomes less significant with a value of  $3.3\sigma$ .

In this section, we report on a multivariate analysis of the kinematics and column density distributions for blue and red galaxies cut by (1) galaxy redshift,  $z_{\text{gal}}$ , and (2) the projected radial distance normalized by the virial radius,  $D/R_{\text{vir}}$ .

#### 4.1. Redshift Evolution

While we find significant differences between blue and red galaxies in the TPCFs in Figure 4(b), the differences may be washed out by other effects. One such effect is the fact that the star formation rate has decreased over time to the present day from a peak at  $z \sim 2-3$  (e.g., Hopkins & Beacom 2006). Therefore, we slice our blue and red subsamples into low and high  $z_{\text{gal}}$ , using a median cut of  $\langle z_{\text{gal}} \rangle = 0.656$ . The mean redshift of the low  $z_{\text{gal}}$  subsample is  $z_{\text{gal}} = 0.469$ , while it is  $z_{\text{gal}} = 0.804$  for the high  $z_{\text{gal}}$  subsample, corresponding roughly to a 2 Gyrs time span between mean redshifts. We present the TPCFs for  $B-K$  and  $z_{\text{gal}}$  subsamples in Figure 6. In the panels, we list the significance of a chi-squared test between subsample pairs as well as the reduced chi-squared value,  $\chi^2_\nu$ , and the degrees of freedom,  $\nu$  for each panel. Mea-

surements of  $\Delta v(50)$  and  $\Delta v(90)$  for each subsample are presented in Table 2.

We find that the TPCF for the red, low  $z_{\text{gal}}$  subsample is an outlier such that it has a significantly smaller velocity dispersion than the rest of the subsamples. In this case, the absorber velocity dispersion for red galaxies evolves with redshift over a span of roughly 2 Gyrs ( $6.5\sigma$ , Figure 6(d)), while there is no such evolution for blue galaxies ( $0.0\sigma$ , Figure 6(c)). At high  $z_{\text{gal}}$  in Figure 6(b), absorption in red galaxies has similar velocity dispersions as in blue galaxies ( $1.8\sigma$ ). However, at lower  $z_{\text{gal}}$  in Figure 6(a), the velocity dispersion for red galaxies decreases, whereas the dispersion for blue galaxies remains constant ( $6.5\sigma$ ). The values of  $\Delta v(50)$  and  $\Delta v(90)$  for all TPCFs are consistent within uncertainties ( $\sim 75 \text{ km s}^{-1}$  and  $\sim 190 \text{ km s}^{-1}$ , respectively) except the red, low  $z_{\text{gal}}$  subsample, which has smaller values than the rest of the subsamples ( $\sim 50 \text{ km s}^{-1}$  and  $\sim 120 \text{ km s}^{-1}$ , respectively) and thus confirms the low velocity dispersions.

In the panels above we plot the cloud column density distributions for the same subsamples as those in the

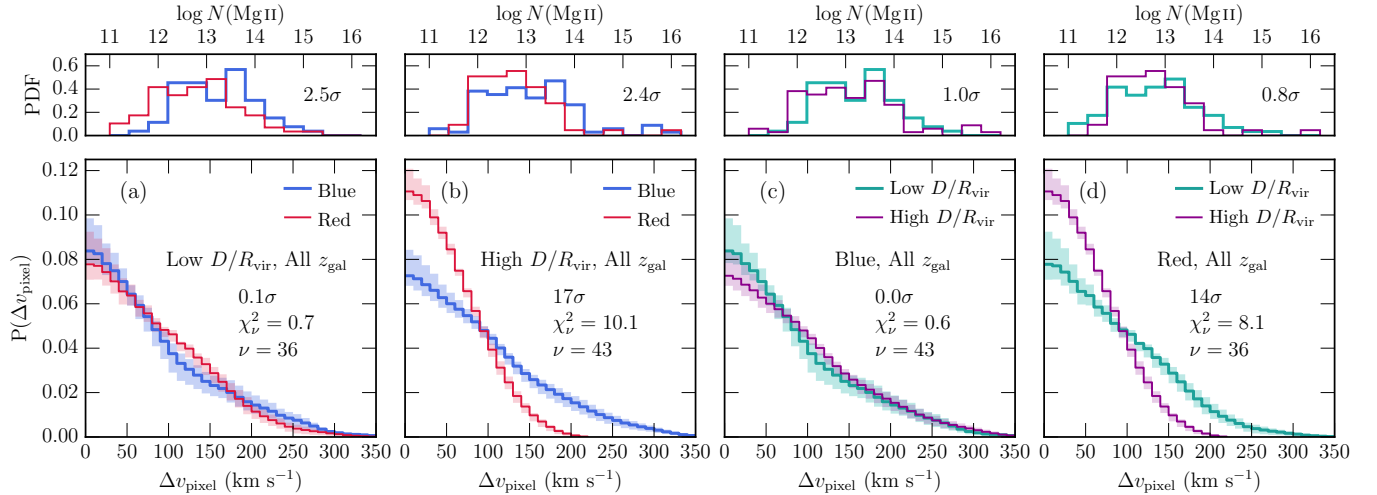


**Figure 8.** Pixel-velocity two-point correlation functions for subsamples sliced by galaxy color,  $B-K$ , and virial radius-normalized impact parameter,  $D/R_{\text{vir}}$ , in the lower panels. Lines, shading, and chi-squared test results are similar to those listed in Figure 6. We find that the red, low  $D/R_{\text{vir}}$  subsample is a significant outlier such that it has a smaller absorber velocity dispersion than either blue galaxies ( $17\sigma$  in panel (b)) or red, high  $D/R_{\text{vir}}$  galaxies ( $14\sigma$  in panel (d)). Upper panels display the differences between cloud column density distributions for the same subsamples plotted in the TPCF panels. KS test results between plotted distributions are noted in each panel. We find no dependence of the cloud column densities with color and  $D/R_{\text{vir}}$ .

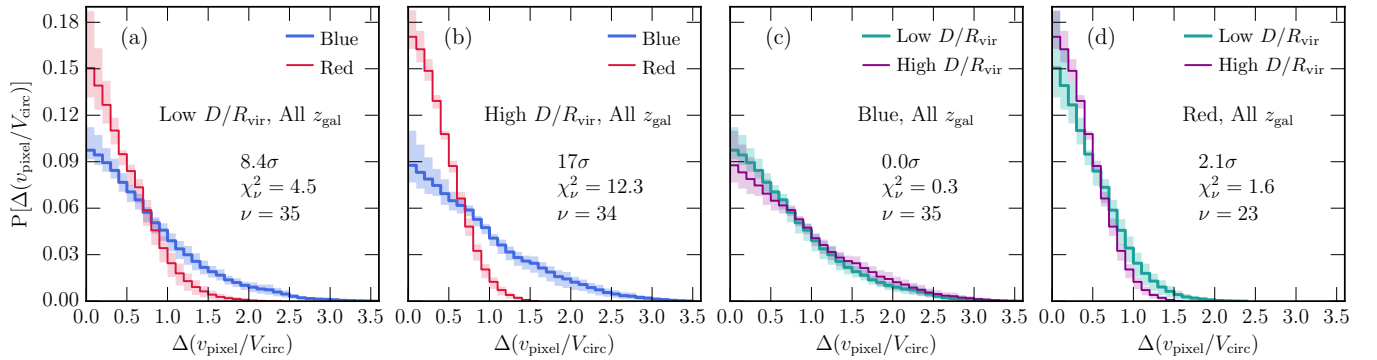


**Figure 9.** Mass-normalized TPCFs for the subsamples plotted in Figure 8. Contrary to the results with the unnormalized absorber TPCFs, we find no dependence on  $D/R_{\text{vir}}$  for either blue or red galaxies in panels (c) and (d), respectively, however red galaxies have smaller absorber velocity dispersions than blue galaxies at all  $D/R_{\text{vir}}$  (panels (a) and (b)).

TPCF plots. The listed significance is the result of a KS test between plotted subsamples. The outlying subsample in these panels is the red, high  $z_{\text{gal}}$  subsample which has smaller values of  $\log N(\text{Mg II})$  than both the blue, high  $z_{\text{gal}}$  subsample ( $4.9\sigma$ , panel (b)), and the red, low  $z_{\text{gal}}$  subsample ( $4.1\sigma$ , panel (d)). We find no difference between the column density distributions associated with blue and red galaxies at low  $z_{\text{gal}}$  ( $0.8\sigma$ , panel (a)) nor do we find redshift evolution in the column density distributions for blue galaxies ( $1.6\sigma$ , panel (c)).

Figure 7 presents TPCFs in which the pixel velocities have been normalized by the circular velocity of the host galaxy. Plotted subsamples are the same as those in Figure 6. We do not plot the column density distributions above these TPCF panels because the act of normalizing the velocities by  $V_{\text{circ}}$  does not affect the column densities. In general, we find the same results for the normalized TPCFs as we did in the unnormalized TPCFs. However, we find that the redshift evolution present in the red galaxies (panel (d)) is no longer as strong as it was when the pixel velocities were not normalized ( $3.3\sigma$ ). For both low and high  $z_{\text{gal}}$ , red galaxies tend to host absorbers with lower velocity dispersions than blue galaxies at the  $14\sigma$  (panel (a)) and  $9.5\sigma$  (panel (b)) levels, respectively. Lastly,

we find that the velocity dispersion of absorbers hosted by blue galaxies does not evolve with redshift with a  $0\sigma$  significance in panel (c).

*To summarize*, we find redshift evolution in both the velocity dispersions and cloud column densities for absorbers associated with red galaxies. However, the sense of the evolution is reversed in that the velocity dispersion decreases from higher to lower  $z_{\text{gal}}$ , while the column densities increase for the same time span. We find no evolution in either the velocity dispersion or the cloud column densities for absorbers associated with blue galaxies.

#### 4.2. Radial Dependence

Another effect that may be washing out differences in the TPCFs of blue and red galaxies is the projected radial distance at which absorption is found. Many previous works have studied the well-known anti-correlation between  $W_r(2796)$  and  $D$ , which is significant to the  $7.9\sigma$  level (see Nielsen et al. 2013b, and references therein). Furthermore, since galaxies span a range of masses, Churchill et al. (2013a) normalized  $D$  by the virial radius to account for the mass of the host galaxy and found an even stronger anti-correlation between  $W_r(2796)$  and  $D/R_{\text{vir}}$  ( $8.9\sigma$ ) (also see Churchill et al. 2013b).

Since  $W_r(2796)$  depends on column densities and/or velocity spreads, examining the TPCFs and cloud column densities as a function of  $D/R_{\text{vir}}$  may provide insight into what aspect of the gas physics gives rise to the  $W_r(2796)$  and  $D/R_{\text{vir}}$  anti-correlation. Therefore, we present TPCFs for subsamples sliced by median values of  $\langle B-K \rangle = 1.4$  and  $\langle D/R_{\text{vir}} \rangle = 0.24$  in Figure 8. The corresponding  $\Delta v(50)$  and  $\Delta v(90)$  measurements are listed in Table 2.

We find that the internal velocity dispersion of absorbers (TPCF) around blue galaxies does not depend on where the absorbers are located in projected distance away from the galaxy ( $0\sigma$ , panel (c)), except the dispersion does if the absorbers are located around red galaxies ( $14\sigma$ , panel (d)). In red galaxies, the internal dispersion of absorbers at low  $D/R_{\text{vir}}$  is comparable to absorbers in blue galaxies, regardless of where they are being probed ( $0.1\sigma$ , panel (a)). The outlier of these TPCFs is the high  $D/R_{\text{vir}}$ , red galaxy subsample, which has a significantly smaller velocity dispersion than for blue, high  $D/R_{\text{vir}}$  galaxies ( $17\sigma$ , panel (b)), or for red, low  $D/R_{\text{vir}}$  galaxies ( $14\sigma$ , panel (d)). These results are also represented in the  $\Delta v(50)$  and  $\Delta v(90)$  measurements, where all subsamples but the red, high  $D/R_{\text{vir}}$  subsample have values of  $\Delta v(50)$  and  $\Delta v(90)$  that are consistent within uncertainties ( $\sim 70 \text{ km s}^{-1}$  and  $\sim 190 \text{ km s}^{-1}$ , respectively). The red, high  $D/R_{\text{vir}}$  subsample has values that are lower than the rest of the subsamples ( $\Delta v(50) \sim 50 \text{ km s}^{-1}$  and  $\Delta v(90) \sim 110 \text{ km s}^{-1}$ ). We note that, although these results are similar to those examining redshift evolution in which one subsample is a clear outlier from the rest, we find no significant anti-correlation from a Kendall- $\tau$  rank correlation test between  $z_{\text{gal}}$  and  $D/R_{\text{vir}}$  ( $2.0\sigma$ ).

The column density distributions for the TPCF subsamples are plotted above each panel in Figure 8. Unlike the galaxy color and redshift subsamples, we find no differences in the column densities with color or  $D/R_{\text{vir}}$ . The largest significance from a KS test is between blue and red galaxies at low  $D/R_{\text{vir}}$  with  $2.5\sigma$ , where red galaxies may tend to have smaller cloud column distributions than blue galaxies. This trend may also be present at high  $D/R_{\text{vir}}$  with a  $2.4\sigma$  significance. Comparing low and high  $D/R_{\text{vir}}$  for blue galaxies and red galaxies, we find insignificant results from the KS test, with  $1.0\sigma$  and  $0.8\sigma$ , respectively.

We present the TPCFs normalized by the host galaxy virial radius in Figure 9 for the same  $B-K$  and  $D/R_{\text{vir}}$  subsamples as in Figure 8. Here we find that red galaxies have lower velocity dispersions than blue galaxies at all  $D/R_{\text{vir}}$ , with a significance level of  $8.4\sigma$  at low  $D/R_{\text{vir}}$  in panel (a) and  $17\sigma$  at high  $D/R_{\text{vir}}$  in panel (b). The  $\Delta v(50)$  and  $\Delta v(90)$  values for these subsample pairs are also not consistent within uncertainties, where the  $\Delta v(50)$  values for blue galaxies ( $\sim 0.6$ ) are roughly twice as large as those for red galaxies ( $\sim 0.3$ ) for all  $D/R_{\text{vir}}$ . In panel (c) we find no difference in the TPCFs with  $D/R_{\text{vir}}$  for blue galaxies ( $0\sigma$ ), with  $\Delta v(50)$  and  $\Delta v(90)$  ( $\sim 0.6$  and  $\sim 1.65$ , respectively) echoing this result. Finally, in panel (d), we find no significant difference in the TPCFs for red galaxies with  $D/R_{\text{vir}}$  ( $2.1\sigma$ ); however, we find that, while  $\Delta v(50)$  is consistent within uncertainties for the two subsamples ( $\Delta v(50) \sim 0.3$ ), the  $\Delta v(90)$  is larger for the low  $D/R_{\text{vir}}$  subsample ( $0.95$ ) than the high  $D/R_{\text{vir}}$  subsample ( $0.75$ ).

In summary, the absorber velocity dispersion depends on  $D/R_{\text{vir}}$  for red galaxies only, where the dispersions are smaller at larger  $D/R_{\text{vir}}$ , and this difference is present only in the tails for the normalized TPCFs. At low  $D/R_{\text{vir}}$ , the velocity dis-

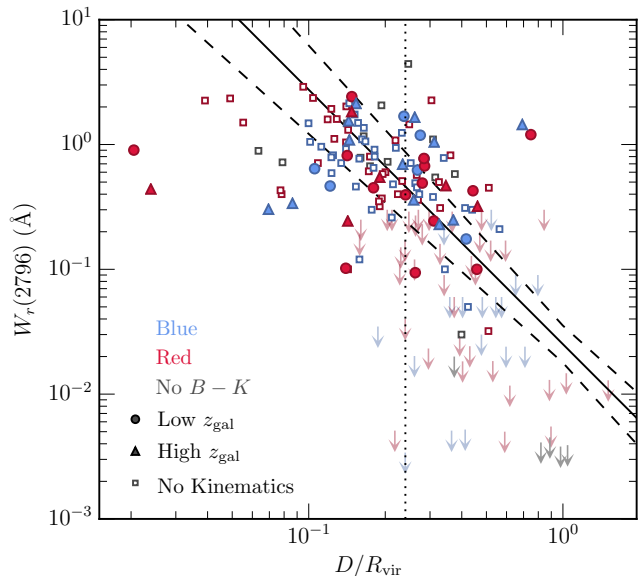


**Figure 10.** MgII equivalent width,  $W_r(2796)$ , versus  $D/R_{\text{vir}}$ . Point colors indicate galaxy color sliced by  $\langle B-K \rangle = 1.4$ . Solid filled points are those galaxies included in the sample presented here. Open points are the rest of the MAGIIICAT (Nielsen et al. 2013b) absorber sample that do not have high resolution quasar spectra. Point types for the kinematics sample represent  $z_{\text{gal}}$ , with circles for low  $z_{\text{gal}}$  and triangles for high  $z_{\text{gal}}$ . Downward arrows are the nonabsorbing galaxies in the MAGIIICAT sample. Solid and dashed lines are the fit to the data obtained by Churchill et al. (2013a). The vertical dotted line is the median  $D/R_{\text{vir}}$  of the kinematics sample, with  $\langle D/R_{\text{vir}} \rangle = 0.24$ . While the full MAGIIICAT sample is anti-correlated to the  $8.9\sigma$  level (Churchill et al. 2013a,b), the kinematics sample (solid points) is not, with a significance of  $0.8\sigma$ .

persions for absorption associated with blue and red galaxies are comparable in the unnormalized TPCFs. In contrast, the cloud column densities do not depend on whether the absorption is located around blue or red galaxies, nor do they depend on  $D/R_{\text{vir}}$ .

### 4.3. Anti-correlation of $W_r(2796)$ and $D/R_{\text{vir}}$

The results presented in the previous section (Section 4.2) are puzzling given the anti-correlation between  $W_r(2796)$  and  $D/R_{\text{vir}}$  (Churchill et al. 2013a,b). Since equivalent width correlates with the number of clouds (Petitjean & Bergeron 1990; Churchill et al. 2003; Evans 2011), the column densities, the velocity spreads, or both should diminish with increasing  $D/R_{\text{vir}}$ . Therefore, we expected that the TPCFs and/or the cloud column densities would show a dependence on  $D/R_{\text{vir}}$  regardless of color where the cloud column densities and/or TPCF velocity dispersions would decrease with increasing  $D/R_{\text{vir}}$ . However, this is not the case. We found no dependence of the TPCF velocity dispersions on  $D/R_{\text{vir}}$  for blue galaxies, but the velocity dispersion for red galaxies is lower at high  $D/R_{\text{vir}}$  (as might be expected) in the unnormalized TPCFs. However, the red galaxy TPCF  $D/R_{\text{vir}}$  dependence vanished when we normalized the pixel velocities by  $V_{\text{circ}}$ . Additionally, the cloud column density distributions do not differ with  $D/R_{\text{vir}}$  for both blue and red galaxies.

To better understand the sample examined here in the context of the  $W_r(2796)$ - $D/R_{\text{vir}}$  anti-correlation, we present Figure 10 in which we plot the present sample of galaxies as solid points, the rest of the MAGIIICAT sample (Nielsen et al. 2013b) absorbing galaxies as open points, and MAGIIICAT nonabsorbing galaxies as downward arrows as their absorp-

tion is only known to a  $3\sigma$  upper limit. This plot is similar to Figure 1(c) in Churchill et al. (2013a), though point colors here represent galaxy colors sliced by the median color,  $\langle B-K \rangle = 1.4$ . The solid and dashed lines are the fit to the data in Churchill et al. (2013a). For reference we plot the median  $D/R_{\text{vir}}$  as a vertical dotted line.

As reported by Churchill et al. (2013a), the anti-correlation is significant to the  $8.9\sigma$  level for the full MAGIIICAT sample using a BHK- $\tau$  non-parametric rank correlation test to account for the upper limits on absorption. Since we study only those systems with detected absorption in high resolution quasar spectra, we ran a Kendall- $\tau$  rank-correlation test between  $W_r(2796)$  and  $D/R_{\text{vir}}$  for the present sample (filled points) and found an anti-correlation that is significant to the  $0.8\sigma$  level. Thus the data presented here do not exhibit an anti-correlation between  $W_r(2796)$  and  $D/R_{\text{vir}}$  (however, if we examine *all* absorbers in the MAGIIICAT sample, we do find an anti-correlation with  $4.6\sigma$  significance). If we examine only blue galaxies, the significance drops further to  $0.2\sigma$  (for red galaxies the significance remains at  $0.8\sigma$ ). This result is then consistent with no  $D/R_{\text{vir}}$  dependence for the cloud column densities regardless of galaxy color and for the TPCFs of blue galaxies. However, it does not explain the differences in the TPCFs of absorbers associated with red galaxies in the unnormalized TPCFs.

We also examined the statistics on this anti-correlation for low and high  $z_{\text{gal}}$  subsamples to determine if the anti-correlation was affecting the redshift evolution results in the TPCFs. Point types in Figure 10 represent  $z_{\text{gal}}$  subsamples, with circles for low  $z_{\text{gal}}$  and triangles for high  $z_{\text{gal}}$ . The Kendall- $\tau$  rank-correlation test resulted in an insignificant anti-correlation between  $W_r(2796)$  and  $D/R_{\text{vir}}$  for both the low  $z_{\text{gal}}$  ( $1.1\sigma$ ) and the high  $z_{\text{gal}}$  ( $0.1\sigma$ ) subsamples.

To ensure that our kinematics sample is not unusual, we randomly drew 39 absorbers from the full MAGIIICAT absorber sample for one million realizations and ran the rank-correlation test each time. The fraction of realizations in which the anti-correlation between  $W_r(2796)$  and  $D/R_{\text{vir}}$  is significant (i.e., the significance is greater than  $3\sigma$ ) is 25%. For blue galaxies (19 absorbers) and similarly with red galaxies (20 absorbers), this fraction drops to 4%. Finding no significant anti-correlation is not unusual. Given the history of absorber-galaxy studies (see e.g., Churchill et al. 2005; Nielsen et al. 2013b, for a list of references), this is not unexpected. With larger numbers of absorber-galaxy pairs, the statistics on the  $W_r(2796)$ - $D$  anti-correlation has steadily become more significant. The main reason for the lack of an anti-correlation for a given smaller sample is the large scatter in the relation.

## 5. DISCUSSION

By examining the kinematics and cloud column densities of MgII absorbers, we have observed redshift evolution in the CGM of red galaxies where the velocity dispersions of absorbers decrease and the cloud column densities increase with decreasing redshift. When examining the kinematics as a function of  $D/R_{\text{vir}}$ , we also find a difference for red galaxies where the velocity dispersions decrease with increasing  $D/R_{\text{vir}}$ , though the cloud column densities do not differ at low and high  $D/R_{\text{vir}}$ . The radial dependence in the velocity dispersions for red galaxies is removed when we normalize the pixel velocities by  $V_{\text{circ}}$ . Conversely, we find no redshift or radial dependence of the velocity dispersions and cloud column densities for blue galaxies. Compared to the red galaxies, the

blue galaxy velocity dispersions and cloud column densities are larger than for red galaxies.

We found that red galaxies have smaller velocity dispersions than blue galaxies overall; this is most obvious in Figure 4. Since blue (less massive) galaxies tend to have a larger star formation rate than red (more massive) galaxies, blue galaxies are more likely to experience outflows than red galaxies. Thus, the large velocity dispersions in blue galaxies may well be due to outflows induced by star formation which act to “stir up” the MgII absorbers, whereas a lack of outflows in red galaxies likely causes the smaller velocity dispersions in red galaxy TPCFs. This is consistent with previous works in which outflows were invoked to explain the presence and properties of MgII absorption (e.g., Rubin et al. 2010, 2014; Bouché et al. 2012; Martin et al. 2012; Bordoloi et al. 2014a,b; Kacprzak et al. 2014).

A possible alternative explanation for the large TPCF velocity dispersions for the blue galaxies is the presence of merging satellite galaxies. Regardless of the host galaxy type, satellite galaxies present such a small cross-section that they are unlikely to be a significant source of MgII absorption around host galaxies. Several works have investigated this by comparing the estimated satellite cross-sections from simulations to the observed incidence of absorption and found that the satellite cross-sections are much lower than the absorption incidence rate (e.g., Tumlinson et al. 2013; Gauthier et al. 2010). Thus, satellites are unlikely to explain the properties of the MgII absorbers we present here. For more discussion of possible effects of satellite contributions to MgII kinematics, see Paper V of the MAGIIICAT series (Nielsen et al. 2015).

That we find differences in the velocity dispersions and cloud column densities for absorbers around red galaxies with redshift, but no such evolution in blue galaxies, may suggest we are observing the consequences of quenched star formation in red galaxies but ongoing star formation in blue galaxies. Due to the ongoing star formation in blue galaxies, the absorbers are likely to be involved in outflows, accretion, and/or recycling at all redshifts, thus their velocity dispersions remain large and their cloud column densities remain unchanged. Outflows may continually replenish the CGM of disturbed, large column density gas.

At high redshift in Figure 6(b), the absorber velocity dispersions are similar regardless of galaxy color, indicating that the red galaxies we observe in the high redshift subsample may have undergone star formation driven outflows recently. At low redshift in Figure 6(a), the TPCFs are narrower for red galaxies than blue, possibly indicating that the outflows at higher redshift have since shut off. This is also shown in the normalized TPCFs in Figure 7, where the high  $z_{\text{gal}}$ , red galaxy TPCF is more narrow than the blue galaxy TPCF, but this difference increases for low  $z_{\text{gal}}$  subsamples. Since the cloud column densities of red galaxies at high  $z_{\text{gal}}$  are smaller than those for blue galaxies, some mechanism present only in red galaxies may break the clouds into smaller column density clouds. At lower redshift, the cloud column density distributions for blue and red galaxies are comparable, but similar to the distribution for blue galaxies at higher redshift.

The quenching of star formation may act to slowly reduce the velocity dispersion of MgII absorbers, but the quenching event initially breaks the clouds into smaller column density clouds, which then increase over time. This may be explained by a scenario in which star forming galaxies have outflows driven by active star formation which agitate and disperse the gas in the CGM to larger velocity dispersions. Star formation



is then shut off via an unknown quenching mechanism (either AGN activity, intense star formation, a galaxy–galaxy merger, etc.) which breaks the clouds into smaller column densities. Over time, the absorbers are allowed to settle to lower velocity dispersions, which then allows for the individual clouds to “re-condense” to form larger column density clouds. Alternatively, the cloud column densities may appear to increase because as the velocity dispersion decreases, the gas builds over a narrower velocity range, resulting in larger measured column densities even if the individual clouds are physically separate with unchanging column densities. Thus the CGM becomes quiescent.

Initially we found a dependence of the red galaxy TPCFs on  $D/R_{\text{vir}}$  where the velocity dispersion decreases with increasing  $D/R_{\text{vir}}$ , which would follow from the  $W_r(2796)$ – $D/R_{\text{vir}}$  anti-correlation discussed in Churchill et al. (2013a). This result and the lack of a dependence of the TPCFs for blue galaxies on  $D/R_{\text{vir}}$  would suggest that outflows push disturbed material out to large distances. Then when star formation is quenched, the velocity dispersions of gas in the inner CGM remain large, but the outer region of the CGM is the first to show signs of quenched star formation in the form of decreasing velocity dispersions. However, by investigating the  $W_r(2796)$ – $D/R_{\text{vir}}$  relation in Section 4.3 we found that there is no anti-correlation for the sample presented here with a  $0.8\sigma$  significance (same for red galaxies) nor blue galaxies whose significance drops to  $0.2\sigma$ . This is likely due to the small sample size as well as the fact that we focus only on absorbers, which have only a  $4.6\sigma$  anti-correlation, compared to the full sample that includes nonabsorbers with  $8.9\sigma$ . Since the  $W_r(2796)$ – $D/R_{\text{vir}}$  anti-correlation is not interfering with, nor contaminating the sample presented here, the redshift evolution of the TPCFs and cloud column densities is more strongly explained as being due to the quenching of star formation rather than an underlying sample bias.

Since the most significant differences in the TPCFs with  $D/R_{\text{vir}}$  were for red galaxies and we have no  $W_r(2796)$ – $D/R_{\text{vir}}$  anti-correlation for this sample, we examined the mass distributions for each of the  $B$ – $K$  and  $D/R_{\text{vir}}$  subsample combinations. We found that galaxies in the low  $D/R_{\text{vir}}$  subsamples tend to be slightly more massive than those in the high  $D/R_{\text{vir}}$  subsamples, for both blue and red galaxies. Thus, normalizing the pixel velocities in the TPCFs by  $V_{\text{circ}}$  removes the mass bias with velocity, where more massive galaxies can have higher velocity gas. Doing this resulted in no differences in the mass-normalized TPCFs with  $D/R_{\text{vir}}$  for both blue and red galaxies. However, the TPCFs for red galaxies are still narrower than for blue galaxies at all  $D/R_{\text{vir}}$ . This may indicate that, after accounting for the mass of the galaxy in both the size of the CGM and velocities, the quenching of star formation in red galaxies affects gas in the CGM at all  $D/R_{\text{vir}}$ , at least out to  $D/R_{\text{vir}} = 0.75$ .

While our findings here provide interesting details into the nature of the CGM, a large body of work has shown that the characteristics of the absorbing gas in the CGM depend on both the galaxy inclination and whether the absorption is located along the galaxy projected major or minor axes (e.g., Bordoloi et al. 2011, 2014b; Bouché et al. 2012; Kacprzak et al. 2010, 2012a; Lan et al. 2014; Rubin et al. 2014). This is especially true for star forming galaxies as outflowing gas tends to be found along the minor axes (e.g., Bouché et al. 2012; Kacprzak et al. 2014) while accretion tends to be detected along the major axes (e.g., Kacprzak et al. 2010; Bouché et al. 2013). These trends have also been observed in

simulations (e.g., Stewart et al. 2011; Danovich et al. 2012, 2015). In the data presented here, there may be hints of a bimodality for the blue galaxy subsample TPCFs and cloud column density distributions, which may be due to these orientation effects. In fact, we examined these orientation effects in a companion paper (MAGIICAT V; Nielsen et al. 2015) and found that the largest velocity dispersions were associated with blue, face-on galaxies ( $i < 57^\circ$ ), and are likely due to outflowing gas pointed towards the observer. The smallest velocity dispersions were associated with red, face-on galaxies, which may be due to a lack of outflows as the star formation in red galaxies has been quenched. Similar velocity dispersions for blue and red galaxies that are in edge-on inclinations ( $i \geq 57^\circ$ ), probed along the galaxy projected major axis, indicated that the gas we observed was accreting/rotating around the galaxies. These orientation results have larger significances in the chi-squared results than the results we present here. Thus, the orientation of the host galaxy may be more important than  $z_{\text{gal}}$  and  $D/R_{\text{vir}}$  in understanding the processes giving rise to absorption in the CGM.

## 6. SUMMARY AND CONCLUSIONS

Using a subset of MAGIICAT galaxies (Nielsen et al. 2013b), we examined the kinematics of gas in the CGM as a function of galaxy color, redshift, and virial radius-normalized impact parameter. Each galaxy was spectroscopically identified to be located at the redshift of an associated MgII absorber in a high-resolution quasar spectrum within a projected distance of  $D = 200$  kpc. Thus the galaxy sample is an absorption-selected sample, and only those absorption regions with  $W_r(2796) \geq 0.04 \text{ \AA}$  were included in our analysis. Galaxy virial radii and circular velocities were obtained using halo abundance matching (Churchill et al. 2013b) and were used to normalize out any mass dependence with impact parameter and velocity.

Our main conclusions are as follows:

1. We find no redshift evolution in the kinematics nor cloud column densities for absorbers hosted by blue galaxies. This is possibly due to ongoing star formation, which causes outflows that continue to agitate and disperse the absorbers to form large velocity dispersions. Outflows thus continually replenish the CGM with large column density, high velocity dispersion gas. This result is still true when we normalize the pixel velocities by  $V_{\text{circ}}$  to remove any mass dependence.
2. Conversely, we find redshift evolution in the kinematics for absorbers hosted by red galaxies. The quenching of star formation in red galaxies may shut off outflows, which then may prevent the CGM from being replenished with the large column density, high velocity dispersion gas seen in blue galaxies. Because of this, once star formation has been quenched, absorbers appear to relax into lower velocity dispersions. The quenching mechanism may act to reduce the cloud column densities initially, but the column densities increase towards lower redshifts. Due to the lower velocity dispersions at lower redshifts, the clouds may be able to “re-condense” into larger column density clouds, or appear to increase in column density due to a narrower velocity range over which the clouds are spread, regardless of the physical distance between clouds. This result also stands when we normalize the pixel velocities by  $V_{\text{circ}}$ .

3. Despite an overall anti-correlation between MgII equivalent width and  $D/R_{\text{vir}}$  reported in Churchill et al. (2013b), the sample we present here (those absorbers for which we have high-resolution quasar spectra) does not follow a  $W_r(2796)-D/R_{\text{vir}}$  anti-correlation. This strengthens the result that the kinematics and cloud column densities of red galaxies undergo redshift evolution since an underlying anti-correlation with  $D/R_{\text{vir}}$  is not interfering with the result.
4. Neither the TPCFs nor the cloud column density distributions depend on  $D/R_{\text{vir}}$  when the absorber pixel velocities are normalized by  $V_{\text{circ}}$  (to remove any possible mass bias in the data). This is consistent with the lack of an anti-correlation between  $W_r(2796)$  and  $D/R_{\text{vir}}$ . Since the TPCFs for red galaxies are more narrow than for blue galaxies at all  $D/R_{\text{vir}}$ , this suggests that quenching affects the CGM out to at least  $D/R_{\text{vir}} = 0.75$ .

This work constitutes our first examination of the kinematics of MgII absorbers as a function of galaxy properties. Previous works had examined the kinematics of the absorbers in a variety of ways but had not connected their results to the host galaxy properties, at least in a statistical fashion as is possible with the pixel-velocity TPCFs. In future work and to further understand the kinematics of gas in the CGM as a function of galaxy properties, we will shift the pixel velocities to the galaxy systemic velocity. We will also examine the gas kinematics as a function of star formation rate (SFR), specific SFR, SFR density, and galaxy metallicity.

We thank C. Steidel and J.-R. Gauthier for providing reduced HIRES/Keck quasar spectra. This material is based upon work supported by the National Science Foundation under Grant No. 1210200 (NSF East Asia and Pacific Summer Institutes). N.M.N. was also partially supported through a NMSGC Graduate Fellowship and a Graduate Research Enhancement Grant (GREG) sponsored by the Office of the Vice President for Research at New Mexico State University. G.G.K. acknowledges the support of the Australian Research Council through the award of a Future Fellowship (FT140100933). M.T.M. thanks the Australian Research Council for Discovery Project grant DP130100568 which supported this work. This work is based in part on observations collected at the European Organisation for Astronomical Research in the Southern Hemisphere under ESO programs 076.A-0860, 69.A-0371, 68.A-0170, 075.A-0841, 65.O-0158, 072.A-0346, 074.A-0201, 67.A-0146, 278.A-5048, 076.A-0463, 67.A-0022, and 67.C-0157. Some of the data presented herein were obtained at the W.M. Keck Observatory, which is operated as a scientific partnership among the California Institute of Technology, the University of California and the National Aeronautics and Space Administration. The Observatory was made possible by the generous financial support of the W.M. Keck Foundation.

## REFERENCES

- Barton, E. J., & Cooke, J. 2009, *AJ*, 138, 1817  
 Bergeron, J., & Boissé, P. 1991, *A&A*, 243, 344  
 Bordoloi, R., Lilly, S. J., Kacprzak, G. G., & Churchill, C. W. 2014a, *ApJ*, 784, 108  
 Bordoloi, R., Lilly, S. J., Knobel, C., et al. 2011, *ApJ*, 743, 10  
 Bordoloi, R., Lilly, S. J., Hardmeier, E., et al. 2014b, *ApJ*, 794, 130  
 Bouché, N., Hohensee, W., Vargas, R., et al. 2012, *MNRAS*, 426, 801  
 Bouché, N., Murphy, M. T., Kacprzak, G. G., et al. 2013, *Science*, 341, 50  
 Chen, H.-W., Helsby, J. E., Gauthier, J.-R., et al. 2010, *ApJ*, 714, 1521  
 Churchill, C. W. 1997, PhD thesis, University of California, Santa Cruz  
 Churchill, C. W., Kacprzak, G. G., & Steidel, C. C. 2005, in *IAU Colloq. 199: Probing Galaxies through Quasar Absorption Lines*, ed. P. Williams, C.-G. Shu, & B. Menard, 24–41  
 Churchill, C. W., Nielsen, N. M., Kacprzak, G. G., & Trujillo-Gomez, S. 2013a, *ApJ*, 763, L42  
 Churchill, C. W., Trujillo-Gomez, S., Nielsen, N. M., & Kacprzak, G. G. 2013b, *ApJ*, 779, 87  
 Churchill, C. W., & Vogt, S. S. 2001, *AJ*, 122, 679  
 Churchill, C. W., Vogt, S. S., & Charlton, J. C. 2003, *AJ*, 125, 98  
 Crighton, N. H. M., Hennawi, J. F., & Prochaska, J. X. 2013, *ApJ*, 776, L18  
 Danovich, M., Dekel, A., Hahn, O., Ceverino, D., & Primack, J. 2015, *MNRAS*, 449, 2087  
 Danovich, M., Dekel, A., Hahn, O., & Teysier, R. 2012, *MNRAS*, 422, 1732  
 Dekker, H., D’Odorico, S., Kaufer, A., Delabre, B., & Kotzlowski, H. 2000, in *SPIE Conference Series*, Vol. 4008, *Optical and IR Telescope Instrumentation and Detectors*, ed. M. Iye & A. F. Moorwood, 534–545  
 Evans, J. L. 2011, PhD thesis, New Mexico State University  
 Fox, A. J., Bordoloi, R., Savage, B. D., et al. 2015, *ApJ*, 799, L7  
 Gauthier, J.-R., Chen, H.-W., & Tinker, J. L. 2010, *ApJ*, 716, 1263  
 Guillemin, P., & Bergeron, J. 1997, *A&A*, 328, 499  
 Hopkins, A. M., & Beacom, J. F. 2006, *ApJ*, 651, 142  
 Kacprzak, G. G., Churchill, C. W., Ceverino, D., et al. 2010, *ApJ*, 711, 533  
 Kacprzak, G. G., Churchill, C. W., Evans, J. L., Murphy, M. T., & Steidel, C. C. 2011, *MNRAS*, 416, 3118  
 Kacprzak, G. G., Churchill, C. W., & Nielsen, N. M. 2012a, *ApJ*, 760, L7  
 Kacprzak, G. G., Churchill, C. W., Steidel, C. C., & Murphy, M. T. 2008, *AJ*, 135, 922  
 Kacprzak, G. G., Churchill, C. W., Steidel, C. C., Spitler, L. R., & Holtzman, J. A. 2012b, *MNRAS*, 427, 3029  
 Kacprzak, G. G., Martin, C. L., Bouché, N., et al. 2014, *ApJ*, 792, L12  
 Lan, T.-W., Ménard, B., & Zhu, G. 2014, *ApJ*, 795, 31  
 Lanzetta, K. M., & Bowen, D. 1990, *ApJ*, 357, 321  
 Lilly, S. J., Carollo, C. M., Pipino, A., Renzini, A., & Peng, Y. 2013, *ApJ*, 772, 119  
 Martin, C. L., Shapley, A. E., Coil, A. L., et al. 2012, *ApJ*, 760, 127  
 Matejek, M. S., & Simcoe, R. A. 2012, *ApJ*, 761, 112  
 Mathes, N. L., Churchill, C. W., Kacprzak, G. G., et al. 2014, *ApJ*, 792, 128  
 Ménard, B., Wild, V., Nestor, D., et al. 2011, *MNRAS*, 417, 801  
 Nielsen, N. M., Churchill, C. W., & Kacprzak, G. G. 2013a, *ApJ*, 776, 115  
 Nielsen, N. M., Churchill, C. W., Kacprzak, G. G., & Murphy, M. T. 2013b, *ApJ*, 776, 114  
 Nielsen, N. M., Churchill, C. W., Kacprzak, G. G., Murphy, M. T., & Evans, J. L. 2015, *ApJ*, 812, 83  
 Oppenheimer, B. D., & Davé, R. 2008, *MNRAS*, 387, 577  
 Petitjean, P., & Bergeron, J. 1990, *A&A*, 231, 309  
 Ribaudo, J., Lehner, N., Howk, J. C., et al. 2011, *ApJ*, 743, 207  
 Rubin, K. H. R., Prochaska, J. X., Koo, D. C., & Phillips, A. C. 2012, *ApJ*, 747, L26  
 Rubin, K. H. R., Prochaska, J. X., Koo, D. C., et al. 2014, *ApJ*, 794, 156  
 Rubin, K. H. R., Weiner, B. J., Koo, D. C., et al. 2010, *ApJ*, 719, 1503  
 Sargent, W. L. W., Steidel, C. C., & Boksenberg, A. 1988, *ApJ*, 334, 22  
 Schneider, D. P., Hartig, G. F., Jannuzi, B. T., et al. 1993, *ApJS*, 87, 45  
 Steidel, C. C., Dickinson, M., Meyer, D. M., Adelberger, K. L., & Sembach, K. R. 1997, *ApJ*, 480, 568  
 Steidel, C. C., Dickinson, M., & Persson, S. E. 1994, *ApJ*, 437, L75  
 Steidel, C. C., Kollmeier, J. A., Shapley, A. E., et al. 2002, *ApJ*, 570, 526  
 Stewart, K. R., Kaufmann, T., Bullock, J. S., et al. 2011, *ApJ*, 738, 39  
 Thom, C., Werk, J. K., Tumlinson, J., et al. 2011, *ApJ*, 736, 1  
 Tumlinson, J., Thom, C., Werk, J. K., et al. 2011, *Science*, 334, 948  
 —. 2013, *ApJ*, 777, 59  
 Vogt, S. S., Allen, S. L., Bigelow, B. C., et al. 1994, in *SPIE Conference Series*, Vol. 2198, *Instrumentation in Astronomy VIII*, ed. D. L. Crawford & E. R. Craine, 362  
 Weiner, B. J., Coil, A. L., Prochaska, J. X., et al. 2009, *ApJ*, 692, 187  
 Werk, J. K., Prochaska, J. X., Thom, C., et al. 2013, *ApJS*, 204, 17